

# Nanoscale self-organisation in Mott insulators: a richness in disguise

**Andrea Ronchi**

Università Cattolica del Sacro Cuore <https://orcid.org/0000-0001-8960-4561>

**Paolo Franceschini**

Università Cattolica del Sacro Cuore

**Andrea De Poli**

Università Cattolica del Sacro Cuore

**Pia Homm**

KU Leuven

**Ann Fitzpatrick**

Diamond Light Source

**Francesco Maccherozzi**

Diamond Light Source, Chilton, Didcot, Oxfordshire, OX11 0DE, UK.

**Gabriele Ferrini**

Università Cattolica del Sacro Cuore <https://orcid.org/0000-0002-5062-9099>

**Francesco Banfi**

Université de Lyon, Université Lyon 1 and CNRS <https://orcid.org/0000-0002-7465-8417>

**Samjeet Dhesi**

Diamond Light Source <https://orcid.org/0000-0003-4966-0002>

**Mariela Menghini**

IMDEA Nanoscience <https://orcid.org/0000-0002-1744-798X>

**Michele Fabrizio**

International School for Advanced Studies (SISSA) <https://orcid.org/0000-0002-2943-3278>

**Jean-Pierre Locquet**

KU Leuven

**Claudio Giannetti** (✉ [claudio.giannetti@unicatt.it](mailto:claudio.giannetti@unicatt.it))

Università Cattolica del Sacro Cuore <https://orcid.org/0000-0003-2664-9492>

---

## Article

**Keywords:** mott transitions, ultrafast light excitation, nanoscale self organization

**Posted Date:** September 10th, 2021

**DOI:** <https://doi.org/10.21203/rs.3.rs-852103/v1>

**License:**  This work is licensed under a Creative Commons Attribution 4.0 International License.

[Read Full License](#)

---

# 1 **Nanoscale self-organisation in Mott insulators: a richness** 2 **in disguise**

3 Andrea Ronchi<sup>1,2,3,†</sup>, Paolo Franceschini<sup>1,2,3</sup>, Andrea De Poli<sup>1,3,4</sup>, Pía Homm<sup>2</sup>, Ann Fitzpatrick<sup>5</sup>,  
4 Francesco Maccherozzi<sup>5</sup>, Gabriele Ferrini<sup>1,3</sup>, Francesco Banfi<sup>6</sup>, Sarnjeet S. Dhesi<sup>5</sup>, Mariela Menghini<sup>2,7</sup>,  
5 Michele Fabrizio<sup>4,\*</sup>, Jean-Pierre Locquet<sup>2</sup> & Claudio Giannetti<sup>1,3,‡</sup>

6 <sup>1</sup>*Department of Physics, Università Cattolica del Sacro Cuore, Brescia I-25121, Italy*

7 <sup>2</sup>*Department of Physics and Astronomy, KU Leuven, Celestijnenlaan 200D, 3001 Leuven, Bel-*  
8 *gium*

9 <sup>3</sup>*ILAMP (Interdisciplinary Laboratories for Advanced Materials Physics), Università Cattolica del*  
10 *Sacro Cuore, Brescia I-25121, Italy*

11 <sup>4</sup>*Scuola Internazionale Superiore di Studi Avanzati (SISSA), Via Bonomea 265, 34136 Trieste,*  
12 *Italy*

13 <sup>5</sup>*Diamond Light Source, Didcot, Oxfordshire, OX11 0DE, UK*

14 <sup>6</sup>*FemtoNanoOptics group, Université de Lyon, CNRS, Université Claude Bernard Lyon 1, Institut*  
15 *Lumière Matière, F-69622 Villeurbanne, France*

16 <sup>7</sup>*IMDEA Nanociencia, Cantoblanco, 28049, Madrid Spain*

17 <sup>†</sup>*andrea.ronchi@unicatt.it*

18 <sup>\*</sup>*fabrizio@sissa.it*

19 <sup>‡</sup>*claudio.giannetti@unicatt.it*

20 **Mott transitions in real materials are first order and almost always associated with lattice**  
21 **distortions, both features promoting the emergence of nanotextured phases. This nanoscale**  
22 **self-organization creates spatially inhomogeneous regions, which can host and protect tran-**  
23 **sient non-thermal electronic and lattice states triggered by light excitation. However, to gain**  
24 **full control of the Mott transition for potential applications in the field of ultrafast switching**  
25 **and neuromorphic computing it is necessary to develop novel spatial and temporal multiscale**  
26 **experimental probes as well as theoretical approaches able to distill the complex microscopic**  
27 **physics into a coarse-grained modelling.**

28 **Here, we combine time-resolved X-ray microscopy, which snaps phase transformations on**  
29 **picosecond timescales with nanometric resolution, with a Landau-Ginzburg functional ap-**  
30 **proach for calculating the strain and electronic real-space configurations. We investigate**  
31  **$V_2O_3$ , the archetypal Mott insulator in which nanoscale self-organization already exists in**  
32 **the low-temperature monoclinic phase and strongly affects the transition towards the high-**  
33 **temperature corundum metallic phase. Our joint experimental-theoretical approach uncov-**  
34 **ers a remarkable out-of-equilibrium phenomenon: the photoinduced stabilisation of the long**  
35 **sought monoclinic metal phase, which is absent at equilibrium and in homogeneous mate-**  
36 **rials, but emerges as a metastable state solely when light excitation is combined with the**  
37 **underlying nanotexture of the monoclinic lattice. Our results provide full comprehension**  
38 **of the nanotexture dynamics across the insulator-to-metal transition, which can be readily**  
39 **extended to many families of Mott insulating materials. The combination of ultrafast light**  
40 **excitation and spatial nanotexture turns out to be key to develop novel control protocols in**

41 **correlated quantum materials.**

## 42 **1 Introduction**

43 Since its original proposal back in 1949 <sup>1</sup>, the Mott metal-insulator transition keeps attracting in-  
44 terest. For long, experimentalists and theorists have put lot of effort to understand the microscopic  
45 bases of such transition in real materials and model Hamiltonians. However, it has recently be-  
46 come urgent to extend that effort towards understanding the dynamics of the Mott transition on  
47 multiple timescales and at length scales much longer than the inter-atomic distances <sup>2</sup>, which are  
48 most relevant for potential applications. Indeed, Mott transitions in real materials have a first order  
49 character, often very pronounced, so that driving across such transitions requires one phase, for-  
50 merly metastable, to nucleate, grow, and finally prevail over the other, formerly stable. In addition,  
51 real Mott transitions are nearly all the times accompanied by a lattice distortion, which, besides  
52 enhancing the first order character of the transition, also constrains the nucleation and growth dy-  
53 namics, fostering the emergence of nanotextures within the insulator-metal coexistence region <sup>3,4</sup>.  
54 Moreover, it may happen that also the lower symmetry crystal structure, usually the insulating  
55 phase, is inhomogeneous because of coexisting twins <sup>5</sup>. This is often the case when the elastic  
56 strain is directly involved in the structural transition.

57       Such circumstances might, at first sight, be regarded just as unwanted side effects that mess  
58 up the Mott transition. In Mott materials, the onset of high-temperature metallicity is accompanied  
59 by the melting of the low-temperature lattice configuration, which is a slow process and implies  
60 a complex real-space rearrangement of domains at the nanoscale. This slow dynamics constitutes

61 the bottleneck for the realization of electronic volatile switches operating at frequencies as high  
62 as several THz <sup>24</sup>, which often discouraged potential applications of insulator-to-metal transitions  
63 (IMT) in real materials either driven by temperature changes or by non-equilibrium protocols such  
64 as light excitation. In this framework, specific efforts have been recently devoted to investigate  
65 possible transient non-thermal states in vanadium oxides, which undergo temperature-driven IMT  
66 of great interest for resistive switching and neuromorphic computing applications <sup>6-23</sup>. Much ac-  
67 tivity has focused on developing strategies to decouple the electronic and structural changes, with  
68 the ultimate goal of achieving all-electronic switching for ultrafast Motronics. The recent claim  
69 of a photoinduced metallic phase of monoclinic VO<sub>2</sub> <sup>25,26</sup> has triggered a huge effort to address  
70 to what extent the photoinduced transition is similar to the thermally driven one and whether the  
71 electronic and lattice degrees of freedom remain coupled at the nanoscale during and after the light  
72 excitation <sup>3,27-30</sup>.

73 The goal of this work is to finally clarify the role of spatial nanotexture in controlling the  
74 Mott transition dynamics and in favouring the decoupling of the electronic and lattice transforma-  
75 tions when the system is driven out-of-equilibrium by light pulses. We focus on the archetypal  
76 Mott insulator V<sub>2</sub>O<sub>3</sub> <sup>31-34</sup>, which indeed realises all at once the full complex phenomenology we  
77 previously outlined, and thus is the privileged playground to attempt such an effort. A nanotex-  
78 tured metal-insulator coexistence across the equilibrium first order transition in thin films has in  
79 fact been observed by near-field infrared microscopy in Ref. 35. Specifically, the metal-insulator  
80 coexistence is characterised by a rather regular array of striped metallic and insulating domains  
81 oriented along two of the three possible hexagonal axes of the high temperature rhombohedral

82 structure, the missing twin possibly being a consequence of the R-plane orientation of the film <sup>36</sup>.  
83 Later, it has been observed, still on thin films but now with a *c*-plane orientation and using X-ray  
84 Photoemission Electron Microscopy (PEEM) <sup>37</sup>, that the monoclinic insulator is itself nanotex-  
85 tured. In particular, such phase looks like a patchwork of the three equivalent monoclinic twins  
86 oriented along the three hexagonal axes of the parent rhombohedral phase. Upon raising the tem-  
87 perature of the monoclinic insulator, metallic domains start nucleating along the interfaces between  
88 the monoclinic twins <sup>37</sup>, thus forming stripes coexisting with insulating ones, all of them again ori-  
89 ented along the hexagonal axes, in agreement with the experiment in Ref. 35. The origin of this  
90 complex nanoscale self-organization, which was tentatively attributed to the long-range Coulomb  
91 repulsion<sup>35</sup>, still remains unexplained.

92 In this work we develop a coarse-grained approach that is able to capture the real-space lattice  
93 and electron dynamics of the IMT in  $V_2O_3$ . Our model demonstrates that the intrinsic nanotexture  
94 is driven by the elastic strain associated to the monoclinic lattice distortion. The full understanding  
95 of the transition dynamics also discloses the possibility of stabilizing a non-thermal metallic elec-  
96 tronic state, which retains the insulating monoclinic lattice structure. This state is unfavorable at  
97 equilibrium and in homogeneous materials, but it can be photoinduced when the electronic popu-  
98 lation within the vanadium *3d* bands is modified by ultrafast light pulses. The intrinsic nanotexture  
99 is key to create the strain conditions at the boundaries of the monoclinic twins, which protect and  
100 stabilize the non-thermal monoclinic metallic phase. We experimentally demonstrate the existence  
101 of such a metastable phase by performing novel synchrotron-based time-resolved X-ray PEEM (tr-  
102 PEEM) experiments with 30 nm and 80 ps spatial and temporal resolution. The excitation of  $V_2O_3$

103 thin films with intense infrared (1.5 eV) ultrashort light pulses turns the material into a metal with  
104 the same shear strain nanotexture of the insulating phase. Even though all experimental and the-  
105 oretical results we are going to present refer to vanadium sesquioxide, they reveal an unexpected  
106 richness that may as well emerge in other Mott insulating materials. The role played by the spon-  
107 taneous nanoscale lattice architectures characterizing first-order IMT provides a new parameter to  
108 achieve full control of the electronic phase transformation in Mott materials.

109         The work is organized as follows. In Sec. 2 we provide an overview of the lattice and elec-  
110 tronic transformations which characterize the phase diagram of  $V_2O_3$ , as well as characterization  
111 of the spontaneous nanotexture of the monoclinic insulating phase. This information is crucial  
112 since it provides the microscopic bases of the multiscale model of the lattice and electronic tran-  
113 sition. In Sec. 3 we introduce the model, based on proper Landau-Ginzburg functionals, and we  
114 show how it captures the nanotexture formation as well as the dynamics of the temperature induced  
115 phase transition. In Sec. 4 we present the central non-equilibrium results. The multiscale model is  
116 extended to treat the non-equilibrium case. The model shows that the nanotexture can favour and  
117 stabilize a non-thermal electronic metallic phase which retains the monoclinic shear strain of the  
118 low-temperature lattice. We experimentally demonstrate this phenomenon by performing tr-PEEM  
119 measurements on  $V_2O_3$  thin films disclosing the ultrafast dynamics with spatial resolution. Finally,  
120 we also show the possibility of controlling the non-thermal transition dynamics by interface strain  
121 engineering.

## 122 2 Electronic and structural transition in $V_2O_3$ : a brief overview

123 **The phase diagram and lattice transformation** The phase diagram of  $(V_{1-x}M_x)_2O_3$ ,  $M=Cr,Ti$ ,  
124 is shown in Fig. 1. It includes rhombohedral paramagnetic insulator and metal phases with corun-  
125 dum structure, and a low temperature dome where the system is a monoclinic antiferromagnetic  
126 Mott insulator. The effect of pressure is, as expected, to favour the metal phase, alike that of Ti  
127 doping, although, above 32.5 GPa, such metal appears to be also monoclinic at room tempera-  
128 ture<sup>38,39</sup>. The low-pressure transition from the high temperature corundum structure to the low  
129 temperature monoclinic one has a first order nature that weakens with Cr doping  $x$ , and maybe  
130 turns continuous above  $x \simeq 0.03$ . For pure  $V_2O_3$ , the case of interest here (dashed vertical line in  
131 Fig. 1) the electronic, magnetic and structural transition that occurs at  $T_c \simeq 170$  K in bulk crystals  
132 has a very pronounced first order character: the jump in resistivity covers almost six orders of  
133 magnitude<sup>32</sup>, and the strain-driven rhombohedral-monoclinic martensitic transformation<sup>40</sup> can be  
134 rather destructive if the sample is not dealt with care.

135 In the rhombohedral phase above  $T_c$ ,  $V_2O_3$  crystallises in a corundum structure, space group  
136  $R\bar{3}c$  No. 167. The non-primitive hexagonal unit cell contains six formula units, and has the lattice  
137 vectors shown in Fig. 2, where<sup>32,41,42</sup>

$$a_H = b_H \simeq 4.936\text{\AA}, \quad c_H \simeq 14.021\text{\AA}, \quad (1)$$

138 and, by convention, we choose  $\mathbf{a}_H \parallel \mathbf{x}$  and  $\mathbf{c}_H \parallel \mathbf{z}$ . The vanadium atoms form honeycomb planes  
139 with ABC stacking, see also the Supplementary Material<sup>43</sup>. It follows that each Vanadium has  
140 only one nearest neighbour along the hexagonal  $\mathbf{c}_H$ -axis. We hereafter denote such vertical pairs as

141 ‘dimers’. Moreover, the two inequivalent V atoms within each honeycomb plane do not lie on such  
 142 plane, see Fig. 2: the atoms that form dimers with the plane above/below are shifted down/up. The  
 143 dimer bond length  $d_0$  is slightly shorter than the distance  $\ell_0$  between nearest neighbour V atoms  
 144 within the hexagonal planes, specifically

$$d_0 \simeq 2.7\text{\AA}, \quad \ell_0 \simeq 2.873\text{\AA}. \quad (2)$$

145 Such difference reflects a trigonal distortion of the oxygen octahedra surrounding each vanadium,  
 146 which is responsible of the V-3d  $t_{2g}$  orbital splitting into a lower  $e_g^\pi$  doublet and an upper  $a_{1g}$  sin-  
 147 glet, and is believed to play a crucial role in the Mott metal-insulator transition <sup>44</sup>. In Fig. 3 we  
 148 draw an oversimplified picture of the Mott transition to emphasise the role of the trigonal crystal  
 149 field splitting.

150

151 The magnetic insulator below  $T_c$  has a monoclinic crystal structure, space group  $I2/a$ , No. 15. The  
 152 structural distortion breaks the  $C_3$  rotation symmetry around the  $c_H$ -axis, and can be viewed <sup>41</sup>  
 153 as a rotation of the atoms in a plane perpendicular to one of three hexagonal axes,  $\mathbf{a}_H$ ,  $\mathbf{b}_H$  and  
 154  $-\mathbf{a}_H - \mathbf{b}_H$ . The three choices correspond to equivalent monoclinic structures, which are distin-  
 155 guishable only in reference to the parent corundum state. We shall here choose for simplicity the  
 156  $\mathbf{a}_H \parallel \mathbf{x}$  rotation axis, which becomes the monoclinic primitive lattice vector  $\mathbf{b}_m$ , so that the rota-  
 157 tion occurs in the  $\mathbf{y} - \mathbf{z}$  plane, where the monoclinic lattice vectors  $\mathbf{a}_m$  and  $\mathbf{c}_m$  lie. Concerning  
 158 magnetism, each  $\mathbf{a}_m - \mathbf{c}_m$  plane is ferromagnetic, while adjacent planes are coupled to each other  
 159 antiferromagnetically, see Fig. 4. In other words, the dimers, which do lie in the  $\mathbf{a}_m - \mathbf{c}_m$  plane,  
 160 are ferromagnetic. Similarly, of the three nearest neighbour bonds in the hexagonal plane, the one

161 lying in the  $\mathbf{a}_m - \mathbf{c}_m$  plane of length  $\ell_y$  is therefore ferromagnetic, while the other two, of length  
 162  $\ell_1$  and  $\ell_2$ , are antiferromagnetic, see Fig. 4.

163 Given our choice of the monoclinic twinning, the relation between monoclinic and hexagonal  
 164 lattice vectors<sup>32,41</sup> are graphically shown in Fig. 4. However, for later convenience, we hereafter  
 165 prefer to use a non-primitive pseudo-hexagonal unit cell, see Fig. 5. With such choice the mono-  
 166 clinic phase corresponds to

$$\begin{aligned}
 a_H &\simeq 5.002\text{\AA}, & b_H &\simeq 4.974\text{\AA}, & c_H &\simeq 13.953\text{\AA}, \\
 \alpha &\simeq 91.73^\circ, & \beta &= 90^\circ, & \gamma &\simeq 120.18^\circ,
 \end{aligned}
 \tag{3}$$

167 as opposed to the corundum parameters in Eq. (1), with  $\alpha = \beta = 90^\circ$  and  $\gamma = 120^\circ$ . The  
 168 corundum-to-monoclinic transition is therefore accompanied by a volume expansion of 1.4%<sup>32</sup>,  
 169 as expected across a metal-insulator transition.

170 Considering the nearest neighbour V-V distances in the hexagonal plane,  $\ell_y$ ,  $\ell_1$ , and  $\ell_2$ , and the  
 171 dimer length  $d$ , see Fig. 4, in the monoclinic phase as compared to the rhombohedral one, see  
 172 Eq. (2),  $\ell_y$  grows by 4%,  $d$  by 1.6%, while  $\ell_1$  and  $\ell_2$  are almost unchanged, one is 0.38% shorter and  
 173 the other 0.14% longer. In other words, in accordance with the Goodenough-Kanamori-Anderson  
 174 rules, all ferromagnetic bonds lengthen, the planar one  $\ell_y$  quite a bit more than the dimer.

175 **Spontaneous nanotexture of the monoclinic insulating phase** As described in Ref. 37, equilib-  
 176 rium Photo-Emission Electron Microscopy (PEEM), exploiting X-ray Linear Dichroism (XLD)<sup>46</sup>  
 177 as the contrast mechanism, can be used to investigate the dynamics of the rhombohedral to mono-  
 178 clinic transition in real space. In Fig. 6a we report typical spatially-resolved XLD-PEEM images

179 taken at  $T=100$  K, i.e. fully in the monoclinic insulating phase of  $V_2O_3$ . In this experiment, Linear  
180 Horizontal (LH)  $s$ -polarized X-ray pulses in resonance with the V  $L_{2,3}$ -edge (520 eV) impinge  
181 with  $75^\circ$  incident angle on a 40 nm  $V_2O_3$  film epitaxially grown on a (0001)- $Al_2O_3$  substrate,  
182 therefore with the  $c$ -axis oriented perpendicular to the surface of the film<sup>45</sup>. For each fixed X-rays  
183 polarization (see the grey arrows on top of the images), three different striped insulating nano-  
184 domains, indicated with red, blue and yellow colours, are clearly visible. The stripe-like domains  
185 are oriented along the edges of the vanadium hexagons, with characteristic dimensions of a few  
186 micrometers in length and 200-300 nm in width. The observed spontaneous nanotexture of the  
187 monoclinic phase demonstrates that the minimization of the total elastic energy drives the forma-  
188 tion of domains in which the monoclinic distortion takes place along one of the three equivalent  
189 directions. As extensively discussed in Ref. 37, when the system is heated up and the coexistence  
190 region is entered, rhombohedral metallic droplets start nucleating at the domain boundaries. Upon  
191 further heating up, the domains grow until the insulator-to-metal percolative transition takes place  
192 at a metallic filling fraction of the order of 0.45. The relation between the nature of the striped  
193 insulating domains and the monoclinic lattice vectors can be further appreciated by rotating the  
194 X-ray polarization and plotting the XLD signal in specific regions (pink square, green circle and  
195 yellow triangle in the left panel of Fig. 6a) corresponding to the three different domains. As shown  
196 in Fig. 6b, the XLD signal of the three different domains is phase-shifted by  $60^\circ$  and has a  $180^\circ$   
197 periodicity.

198 To interpret these observations, in Section S5 of the Supplementary Material<sup>43</sup> we calculate  
199 the polarization dependence of the XLD contrast within the monoclinic phase. In brief, the  $a_{1g}$

200 singlet and the  $e_g^\pi$  doublet transform, respectively, as the one dimensional,  $A_1 \sim z^2$ , and two  
 201 dimensional,  $E \sim (x, y)$ , irreducible representations of  $D_3$ . The monoclinic distortion generates a  
 202 mixing between  $a_{1g}$  and the combination of the  $e_g^\pi$  that lies on the  $\mathbf{a}_m - \mathbf{c}_m$  monoclinic plane, i.e.,  
 203 perpendicular to  $\mathbf{b}_m$ . Such combination evidently changes among the three equivalent monoclinic  
 204 twins, and, because of its directionality, it does contribute to the XLD signal, which we find is  
 205 minimum (maximum) for in-plane components of the field parallel (perpendicular) to the  $\mathbf{b}_m$  axis.  
 206 Since the latter can be any of the three hexagonal axes, this immediately explains the observation  
 207 in Fig. 6b, but also allows us to conclude that the interface between two of the three monoclinic  
 208 twins is perpendicular to the  $\mathbf{b}_m$  axis of the third one.

### 209 **3 Multiscale modelling**

210 The self-organization of the monoclinic insulating phase on length scales of the order of hundreds  
 211 nanometers calls for a multiscale theory effort which builds on the microscopic parameters govern-  
 212 ing the transition but goes beyond by describing the formation of domains at length scales much  
 213 larger than the lattice unit cell. Already Denier and Marezio<sup>41</sup> emphasised that the main change  
 214 that occurs across the rhombohedral to monoclinic transition is actually the displacement of the V  
 215 atoms of a dimer towards "the adjacent octahedral voids", see also the Supplementary Material<sup>43</sup>.  
 216 Such displacement results in a  $\theta = 1.8^\circ$  anticlockwise rotation of the dimers around the  $\mathbf{b}_m$  axis,  
 217 thus the value of  $\alpha \simeq 91.73^\circ$  and the  $c_H$  axis compression in Eq. (3). In addition, the dimer elon-  
 218 gates by 1.6%. More specifically, the Vanadium displacement, with our choice of monoclinic axis  
 219  $\mathbf{b}_m \parallel \mathbf{x}$ , has non negligible components along both  $\mathbf{y}$  and  $\mathbf{z}$ , the former leading to the  $1.8^\circ$  dimer

220 tilting, and the latter mostly responsible of the 1.6% stretching of the bond. We remark that the  
221 tilting alone accounts not only for the variations of  $\alpha$  and  $c_H$ , but also for the increase in  $\ell_y$ , which  
222 is the most significant change crossing the structural transition, as well as for the dilation along the  
223 hexagonal  $a_H$ , cf. Eq. (1) with (3). Therefore, the deformation of the unit cell across the transition  
224 is primarily a consequence of the dimer tilting, namely of the Vanadium displacements along  $y$ .

225 Hereafter, we thus make the assumption that the  $y$  and  $z$  components of the Vanadium dis-  
226 placement, or, equivalently, the dimer tilting and its elongation, correspond to different degrees of  
227 freedom, by all means coupled to each other<sup>47</sup>, but each playing its distinctive role. The tilting  
228 is ultimately responsible of breaking the threefold rotation symmetry around  $c_H$ , and thus of the  
229 rhombohedral to monoclinic transition. On the contrary, the V-displacement along  $z$  preserves the  
230  $R\bar{3}c$  space group, but increases the trigonal distortion and, concurrently, reduces the dimer bonding  
231 strength. Both these effects are believed<sup>44</sup> to drive  $V_2O_3$  towards a Mott insulating state, irrespec-  
232 tive of the monoclinic distortion. Similarly, the  $C_3$  symmetry breaking at the structural transition  
233 may not necessarily go along with a metal-insulator transition. DFT-GGA electronic structure cal-  
234 culations predict<sup>48</sup> that the Fermi surface of the corundum metal is unstable towards a monoclinic  
235 distortion. Such weak-coupling Fermi surface instability has its strong coupling counterpart. In-  
236 deed, assuming a Mott insulating state in which each Vanadium acts like a spin-1, see Fig. 3, it was  
237 shown<sup>48</sup> that  $V_2O_3$  realises on each honeycomb plane a highly frustrated Heisenberg model, with  
238 comparable nearest and next-nearest neighbour antiferromagnetic exchange constants<sup>49-51</sup>. Such  
239 frustration is efficiently resolved by the monoclinic distortion stabilising the stripe phase shown in  
240 Fig. 4. This prediction has got further support by recent inelastic neutron scattering data combined

241 with DFT calculations <sup>52</sup>. All the above results suggest that the corundum phase of pure  $V_2O_3$  is  
 242 intrinsically unstable, and destined to turn into a monoclinic phase at low temperature. The fact  
 243 that such transition happens to coincide with a metal to an antiferromagnetic insulator transition  
 244 indicates just a strong positive interplay between the lattice instability and the electronic corre-  
 245 lations <sup>47,48,52</sup>. However, nothing would prevent the structural and the metal-insulator transitions  
 246 to occur separately. Indeed, chromium doping, see Fig. 1, does drive a metal-insulator transition  
 247 without an intervening monoclinic distortion. The opposite case of a monoclinic transition not  
 248 accompanied by a metal-insulator one is still highly debated. Evidences of a monoclinic metal  
 249 phase have been observed in  $V_2O_3$  at high pressure <sup>38,39</sup>. On the contrary, at ambient pressure the  
 250 possible existence of a monoclinic metal phase remains so far controversial <sup>30,35,37,53–58</sup>.

251 The rhombohedral to monoclinic martensitic transformation is therefore driven primarily  
 252 by the dimer tilting, which, macroscopically, corresponds to a lattice strain. We recall that the  
 253 infinitesimal strain tensor is defined as

$$\epsilon_{ij}(\mathbf{r}) = \frac{1}{2} \left( \frac{\partial u_i(\mathbf{r})}{\partial r_j} + \frac{\partial u_j(\mathbf{r})}{\partial r_i} \right), \quad i, j = 1, 2, 3, \quad (4)$$

254 where  $\mathbf{u}(\mathbf{r})$  is the displacement field. It is physically more convenient to define new strain variables

255 through

$$\begin{aligned}
\epsilon &= \frac{\epsilon_{11} + \epsilon_{22}}{2}, & \epsilon_3 &= \epsilon_{33}, \\
\epsilon_1 &= \begin{pmatrix} \frac{\epsilon_{11} - \epsilon_{22}}{2} \\ \epsilon_{12} \end{pmatrix} = \epsilon_1 \begin{pmatrix} \cos \phi_1 \\ \sin \phi_1 \end{pmatrix}, \\
\epsilon_2 &= \begin{pmatrix} \epsilon_{13} \\ \epsilon_{23} \end{pmatrix} = \epsilon_2 \begin{pmatrix} \cos \phi_2 \\ \sin \phi_2 \end{pmatrix},
\end{aligned} \tag{5}$$

256 with  $\epsilon_i = |\epsilon_i| \geq 0$ ,  $i = 1, 2$ , which transform under a rotation around  $z$  by a generic angle  $\phi$

257 according to

$$\begin{aligned}
\epsilon &\rightarrow \epsilon, & \epsilon_1 &\rightarrow \epsilon_1, & \epsilon_2 &\rightarrow \epsilon_2, & \epsilon_3 &\rightarrow \epsilon_3, \\
\phi_1 &\rightarrow \phi_1 + 2\phi, & \phi_2 &\rightarrow \phi_2 + \phi.
\end{aligned} \tag{6}$$

258 The  $C_3$  symmetry of the rhombohedral structure implies invariance only under rotations by  $\phi =$   
259  $\pm 2\pi/3$ .

260 The strain components directly related to the dimer tilting are the shear strain ones,  $\epsilon_{13}$  and  $\epsilon_{23}$ ,  
261 which transform as the components of a planar vector, see Eq. (6). We can therefore identify  
262 the vector  $\epsilon_2$  in (5) with the two-component order parameter of the rhombohedral to monoclinic  
263 transition. Specifically, using the structural data of the corundum and monoclinic structures across  
264 the transition<sup>32,41,42</sup>, and in our reference frame, the shear strain order parameter  $\epsilon_2$  just after  
265 the transition has magnitude  $\epsilon_2 \simeq 0.01756$ , and three possible orientations, i.e., monoclinic twins,  
266 defined by the phases, see Eq. (5),

$$\phi_{2,n} = \frac{\pi}{6} + (n - 1) \frac{2\pi}{3}, \quad n = 1, 2, 3. \tag{7}$$

267 In other words,  $\epsilon_2$  is directed along  $\mathbf{b}_m \wedge \mathbf{c}_H$ . The finite  $\epsilon_2$  in turns drives a finite  $\epsilon_1$ , with magnitude

268  $\epsilon_1 \simeq 0.01337$  and angles,

$$\phi_{1,n} = (2\phi_{2,n} + \pi) \bmod(2\pi), \quad (8)$$

269 implying that  $\epsilon_1$  is parallel to the monoclinic  $\mathbf{b}_m$  axis, as well as finite  $\epsilon \simeq 0.00937 > 0$  and

270  $\epsilon_3 \simeq -0.00487 < 0$ .

271 Apart from assuming that the tilting and stretching of the V-V dimers are distinct degrees of  
272 freedom, we shall here give up any attempt to describe microscopically the rhombohedral to  
273 monoclinic transition in  $\text{V}_2\text{O}_3$ , and instead resort to a more macroscopic approach based on a  
274 Landau-Ginzburg theory for the order parameter that ultimately characterises the structural transi-  
275 tion, namely the shear strain  $\epsilon_2$ , and the one that instead drives the metal-insulator transition, i.e.,  
276 the dimer length  $d$ .

277 **Landau-Ginzburg theory of the structural transition** A Landau-Ginzburg free energy func-  
278 tional for the space dependent order parameter  $\epsilon_2(\mathbf{r})$  is rather cumbersome to derive, since all  
279 other components of the strain, beside the order parameter, are involved, and need to be integrated  
280 out to obtain a functional of  $\epsilon_2(\mathbf{r})$  only. This is further complicated by the constraints due to the  
281 Saint-Venant compatibility equations, which avoid gaps and overlaps of different strained regions  
282 and play a crucial role in stabilising domains below the martensitic transformation<sup>59–61</sup>. Therefore,  
283 not to weigh down the text, we present the detailed derivation of the Landau-Ginzburg functional  
284 in the Supplementary Material<sup>43</sup>, and here just discuss the final result in the  $c$ -plane oriented film  
285 geometry of the experiments.

286 We find that the shear strain two-component order parameter  $\epsilon_2(\mathbf{r})$  is controlled by the energy  
287 functional<sup>43</sup>

$$E[\epsilon_2] = \int d\mathbf{r} \left\{ -\frac{K}{2} \epsilon_2(\mathbf{r}) \cdot \nabla^2 \epsilon_2(\mathbf{r}) + \tau \epsilon_2(\mathbf{r})^2 - \gamma \epsilon_2(\mathbf{r})^3 \sin 3\phi_2(\mathbf{r}) + \mu \epsilon_2(\mathbf{r})^4 \right\} \quad (9)$$

$$+ \kappa \iint d\mathbf{r} d\mathbf{r}' \epsilon_2(\mathbf{r}) \cdot \hat{U}(\mathbf{r} - \mathbf{r}') \epsilon_2(\mathbf{r}'),$$

288 where  $\mathbf{r} = r (\cos \phi, \sin \phi)$  is the two dimensional coordinate of the film,  $\mu$  and  $\kappa$  are positive  
 289 parameters that depend on the elastic constants, while  $\gamma$  is directly proportional to the elastic  
 290 constant  $c_{14}$ <sup>43</sup>. The quadratic coupling constant  $\tau$ , which encodes the electronic effects, drives  
 291 the transition and thus depends critically on temperature; it is positive in the corundum phase and  
 292 negative in the monoclinic one. The last term in (9) derives from the Saint-Venant compatibility  
 293 equations<sup>43</sup>. Specifically,

$$\hat{U}(\mathbf{r}) = \begin{pmatrix} U_{11}(\mathbf{r}) & U_{12}(\mathbf{r}) \\ U_{21}(\mathbf{r}) & U_{22}(\mathbf{r}) \end{pmatrix}, \quad (10)$$

294 where the long-range kernels have the explicit expressions:

$$U_{11}(\mathbf{r}) = -U_{22}(\mathbf{r}) = -\frac{\cos 4\phi}{\pi r^2}, \quad (11)$$

$$U_{12}(\mathbf{r}) = U_{21}(\mathbf{r}) = \frac{\sin 4\phi}{\pi r^2},$$

295 and favour the existence of domains in the distorted structure<sup>59-61</sup>. The orientation of the interfaces  
 296 between those domains is instead determined by the additional constraint we must impose<sup>43</sup> to  
 297 fulfil the Saint-Venant equations, namely the curl free condition

$$\nabla \wedge \epsilon_2(\mathbf{r}) = 0. \quad (12)$$

298 If  $\tau < 0$ , the energy (9) is minimum at the angles defined in Eq. (7) when  $\epsilon_2 > 0$ . The  
 299 constraint (12) implies that a sharp interface between two domains, identified by two of the three

300 possible directions of  $\epsilon_2$ , is oriented along the third one, namely along a mirror plane of the space  
 301 group  $R\bar{3}c$ . This is exactly what is found experimentally, as we earlier discussed.

302 We also note that the minima of the energy functional (9) depend on the values and signs of  $\tau$  and  
 303  $\gamma \propto c_{14}$ . Specifically, the corundum phase,  $\epsilon_2 = 0$ , is a local minimum for  $\tau > \tau_r \gtrsim 0$ ,  $\tau_r$  being the  
 304 rhombohedral spinodal point. Similarly, a monoclinic phase is a local minimum for  $\tau < \tau_m$ , where  
 305 the monoclinic spinodal point  $\tau_m \geq \tau_r$ . Phase coexistence thus occurs when  $\tau \in [\tau_r, \tau_m]$ , and also  
 306 the structural transition must take place at  $\tau_c$  within that same interval. At ambient temperature and  
 307 pressure,  $\tau \sim c_{44} \simeq 53 \text{ eV/cm}^3$ , which must be greater than  $\tau_c$  since the stable phase is corundum,  
 308 and  $c_{14} \simeq -12.5 \text{ eV/cm}^3$ <sup>62-64</sup>, so that  $\gamma$  is negative, too. Well below the structural transition at  
 309 ambient pressure,  $\tau$  must be smaller than  $\tau_r$ , and  $\gamma$  has to become positive in order for  $\epsilon_2$  to have  
 310 the observed values in the monoclinic phase. Therefore, upon lowering the temperature  $T$ ,  $\tau$  must  
 311 decrease, while  $c_{14} \propto \gamma$  must increase and cross zero. There are actually evidences, specifically  
 312 in chromium doped compounds<sup>63</sup>, that  $c_{14}$  does change sign approaching the transition from the  
 313 corundum phase. We are not aware of any experimental measurement of  $c_{14}$  in pure  $\text{V}_2\text{O}_3$  below  
 314 room temperature. Therefore, here we can only conjecture what may happen. One possibility is  
 315 that  $c_{14}$  crosses zero right at the structural transition,  $\tau = \tau_c$ . In such circumstance, the transition  
 316 may become continuous<sup>65</sup>, which is likely the case of Cr doping with  $x \gtrsim 0.03$ <sup>66</sup>. The alternative  
 317 compatible with the ambient pressure phase diagram in Fig. 1 for pure or weakly Ti/Cr doped  $\text{V}_2\text{O}_3$   
 318 is that  $c_{14}$  becomes positive at temperatures higher than  $T_c$ , thus the observed first order transition  
 319 from the corundum phase,  $\epsilon_2 = 0$ , to the monoclinic one,  $\epsilon_2 > 0$ . There is still a third possibility  
 320 that  $\tau$  crosses  $\tau_c$  at high temperature, when  $c_{14} \propto \gamma$  is still negative. In such circumstance, the

321 monoclinic phase that establishes for  $\tau < \tau_c$  corresponds to a shear strain different from that  
322 observed in  $V_2O_3$  at ambient pressure, specifically to a dimer tilting in the clockwise direction or,  
323 equivalently, to opposite  $\epsilon_2$  vectors. This is presumably what happens in the monoclinic metal  
324 phase observed above 32.5 GPa at 300 K <sup>38</sup>.

325 Here, we shall not consider such extreme conditions, and therefore take for granted that, at  
326 ambient pressure and for high temperatures such that  $\gamma$  is negative,  $\tau$  remains greater than  $\tau_c$ , so  
327 that the stable phase is always rhombohedral. Moreover, since we are just interested in pure  $V_2O_3$ ,  
328 we shall assume that  $\gamma$  becomes positive well above the structural transition, around which we  
329 shall therefore consider  $\gamma > 0$  constant, and  $\tau \propto (T - T_0)$ , with  $T_0 > 0$  a parameter, playing the  
330 role of a reduced temperature.

331 **Contribution from the dimer stretching** The energy functional (9) controls only the shear strain  
332  $\epsilon_2$ , namely the dimer tilting. We still need to include the dimer elongation, which is responsible  
333 of the metal-insulator transition <sup>44</sup>. Although the dimer length does not affect substantially the  
334 strain, the dimer tilting does favour its elongation, as discussed, e.g., by Tanaka in <sup>47</sup>. Following  
335 that approach, we assume that for a given tilting angle  $\theta$ , equivalently shear strain  $\epsilon_2$ , the dimer  
336 length  $d$  has two equilibrium positions <sup>47</sup>. However, unlike Tanaka, we associate the two minima  
337 at shorter and longer  $d$  in the metal and insulator phases, respectively. Therefore, replacing  $d$  with  
338 the dimensionless space-dependent field  $\eta(\mathbf{r})$ , we assume the latter to be described by the energy

339 functional

$$\delta E[\epsilon_2, \eta] = a \int d\mathbf{r} \left[ \left( \eta(\mathbf{r})^2 - \frac{1}{4} \right)^2 - g \left( \epsilon_2(\mathbf{r})^2 - \epsilon_{IMT}^2 \right) \eta(\mathbf{r}) \right], \quad (13)$$

340 with  $a > 0$ ,  $g > 0$ , and  $\epsilon_{IMT}^2$  either positive or negative. A minimum at  $\eta < 0$  corresponds to  
341 a metal, while one at  $\eta > 0$  to an insulator, and both may coexist. Note that  $\epsilon_2^2 > \epsilon_{IMT}^2$  implies  
342 that the global minimum is insulating, whereas  $\epsilon_2^2 < \epsilon_{IMT}^2$  that is metallic. In other words,  $\epsilon_{IMT}^2$   
343 represents the threshold strain above which an insulating phase becomes stable.

344 **Total energy functional** Adding the shear strain energy  $E[\epsilon_2]$  in Eq. (9) to the dimer stretching  
345 contribution  $\delta E[\epsilon_2, \eta]$  in Eq. (13), we obtain the total energy functional

$$E[\epsilon_2, \eta] = E[\epsilon_2] + \delta E[\epsilon_2, \eta], \quad (14)$$

346 which can actually describe rhombohedral and monoclinic phases, either metallic or insulating.

347

348 For instance, assuming  $\epsilon_{IMT}^2 < 0$  in Eq. (13), the energy functional (14) predicts a transition  
349 from a rhombohedral insulator to a monoclinic one upon lowering  $T$ , i.e., the reduced temperature  
350  $\tau$ , as indeed observed above 1% of Cr doping, see Fig. 1.

351 Pure  $V_2O_3$  corresponds instead to assuming  $\epsilon_{IMT}^2 > 0$ . In this case, the stable rhombohedral  
352 phase, with  $\epsilon_2 = 0$ , is metallic. Upon crossing the first order structural transition at  $T = T_c$ ,  $\epsilon_2$   
353 jumps directly to a finite value,  $\epsilon_2(T_c)$ , which grows upon further lowering  $T$ . If we assume, in  
354 agreement with the most recent experimental claims<sup>58</sup>, that at equilibrium there is no monoclinic  
355 metal phase in between the rhombohedral metal and monoclinic insulator, we must conclude that

356 just after the transition to the monoclinic phase  $\epsilon_2(T_c)^2 - \epsilon_{IMT}^2 > 0$ , so that the global monoclinic  
 357 minimum is always insulating. Consequently, we fixed the parameters of the energy functional  
 358 so that, assuming homogeneous phases, i.e., neglecting the Ginzburg term and the long range  
 359 potential,  $K = \kappa = 0$  in Eq. (9), the phase diagram, see Fig. 7, shows a direct first order transition  
 360 from a corundum metal to a monoclinic insulator, with a coexistence region of width  $\Delta T = \Delta\tau \simeq$   
 361 40K consistent with experiments. We emphasise that the absence of a stable monoclinic metal does  
 362 not exclude its presence as a metastable phase that is allowed by the energy functional (14), and  
 363 which we indeed find, see Fig. 7.

364 **Domains at equilibrium** We mentioned that the long range elastic potential  $\hat{U}(\mathbf{r})$  in (9) favours<sup>59</sup>  
 365 the existence of domains in the lower symmetry monoclinic phase, which seem to persist also  
 366 within the insulator-metal coexistence region across the first order transition<sup>35,37,57,58</sup>. Since the  
 367 configurational entropy in presence of different domains plays an important role at finite temper-  
 368 ature, we cannot simply search for the minima of the classical energy functional Eq. (14) varying  
 369 the reduced temperature  $\tau$ , as in Fig. 7, but we need to calculate actual thermodynamic averages.  
 370 For that, we take inspiration from the mean field theory developed in Refs. 61, 67, which was  
 371 originally developed for ferroelastic transitions, and we extend it to treat the lattice and electronic  
 372 insulator-to-metal nanotextured dynamics in a Mott material. We discuss thoroughly such mean-  
 373 field scheme in the Supplementary Material<sup>43</sup>, while here we just present the results.

374 In Fig. 8 we show the calculated real space distribution of the shear strain  $\epsilon_2(\mathbf{r})$  at low  
 375 temperature, i.e., deep inside the monoclinic insulator. As expected, the distribution is not homo-

376 geneous, but shows coexistence of equivalent monoclinic twins, each characterised by a colour that  
 377 corresponds to one of the three equivalent shear strain vectors  $\epsilon_{2,i}$ ,  $i = 1, 2, 3$ , see Eq. (7), which  
 378 are shown on the left in Fig. 8. We note that the interface between two domains, i.e., two strain  
 379 vectors  $\epsilon_{2,i}$  and  $\epsilon_{2,j}$ ,  $i \neq j$ , is directed along the third vector,  $\epsilon_{2,k}$ ,  $k \neq i, j$ , in accordance with the  
 380 curl-free condition (12), and with the experimental data presented in Sec. 2. In addition, the strain  
 381 along the interfaces is strongly suppressed as compared to the interior of each domain, as indicated  
 382 by the lighter regions in Fig. 8. The inherent suppression of the strain amplitude at the domain  
 383 boundaries will turn out to play a fundamental role in seeding and stabilizing the photo-induced  
 384 non-thermal metallic phase.

385 In the top panel of Fig. 9 we show the calculated real space distribution of  $\epsilon_2(\mathbf{r})$  within the  
 386 monoclinic-rhombohedral coexistence region across the temperature driven first-order transition,  
 387 where the green colour indicates the rhombohedral domains. The bottom panel of Fig. 9 instead  
 388 shows the real space distribution of  $\epsilon_2(\mathbf{r})^2 = \epsilon_2(\mathbf{r}) \cdot \epsilon_2(\mathbf{r})$ , which is finite in any monoclinic domain,  
 389 and zero in rhombohedral ones. We mentioned that the insulator is locally stable if the shear-strain  
 390 amplitude square  $\epsilon_2(\mathbf{r})^2 > \epsilon_{IMT}^2$ , otherwise the locally stable phase is metallic. For that reason,  
 391 we use in the bottom panel of Fig. 9 a blue colorscale for all regions where  $\epsilon_2(\mathbf{r})^2 > \epsilon_{IMT}^2$ , and  
 392 a red colorscale for  $\epsilon_2(\mathbf{r})^2 < \epsilon_{IMT}^2$ , the two colours thus distinguishing between insulating and  
 393 metallic domains. We note that, as  $T$  raises, metallic domains start to nucleate first with a residual  
 394 monoclinic strain, light red, that soon disappears, dark red. This gives evidence that the metastable  
 395 monoclinic metal does appear across the monoclinic-rhombohedral phase transition, even though  
 396 it gives in to the rhombohedral metal before a percolating metal cluster first sets in, in accordance

397 with experiments <sup>58</sup>.

398 We also observe that rhombohedral domains, dark red, have triangular shapes, as dictated by the  
399 curl-free condition (12) at the interfaces between monoclinic and rhombohedral domains. This  
400 pattern does not resemble the observed experimental one <sup>35</sup>. This difference is due to the  $c$ -plane  
401 orientation that we use, in contrast to the  $A$ -plane one in the experiment <sup>35</sup>.

#### 402 **4 Light-induced non-equilibrium transition: evidence of a transient monoclinic metal phase**

403 **Space-dependent non-equilibrium model** We note that the above theoretical modelling may also  
404 account for the experimental evidences <sup>9,20,21,37</sup> of a photo-induced metal phase in  $V_2O_3$ . As  
405 discussed in Refs. 20, 21, 37, the main effect of the 1.5 eV laser pulse is to transfer electrons from  
406 the  $e_g^\pi$  to the  $a_{1g}$  derived bands, see Fig. 3. The increase in  $a_{1g}$  population at the expense of the  $e_g^\pi$   
407 one leads to a transient reduction of the actual trigonal field splitting between  $e_g^\pi$  and  $a_{1g}$  orbitals,  
408 which depends on their occupations via Coulomb interaction, thus driving the insulator towards the  
409 metal. Such effect of the laser pump can be easily included in the double-well potential (13) that  
410 describes the dimer stretching, i.e., the trigonal splitting, by adding a laser fluence,  $f$ , dependent  
411 term linear in  $\eta$ , namely

$$\delta E[\epsilon_2, \eta] \rightarrow \delta E[\epsilon_2, \eta] + \int d\mathbf{r} \mu(f) \eta(\mathbf{r}), \quad (15)$$

412 with  $\mu(f) > 0$ , being zero at  $f = 0$  and growing with it, thus favouring the metal state with  $\eta < 0$ .

413 This term is actually equivalent to a fluence dependent threshold strain

$$\epsilon_{IMT}^2 \rightarrow \epsilon_{IMT}^2(f) \equiv \epsilon_{IMT}^2 + \mu(f)/g, \quad (16)$$

414 that increases with  $f$ . Looking at the bottom panel of Fig. 9, such upward shift of  $\epsilon_{IMT}(f)$  implies  
415 not only that formerly insulating regions with  $\epsilon_{IMT} < \epsilon_2(\mathbf{r}) < \epsilon_{IMT}(f)$  may turn metallic, but also  
416 the possibility that a laser pulse with a fluence exceeding a threshold value stabilises the formerly  
417 metastable monoclinic metal. Indeed, we earlier mentioned that we fix  $\epsilon_{IMT}$  smaller than the shear  
418 strain amplitude  $\epsilon_2(T_c)$  just after the rhombohedral to monoclinic first order transition, which  
419 ensures the absence of a stable monoclinic metal at equilibrium. After laser irradiation,  $\epsilon_{IMT}(f)$   
420 may well surpass the shear strain amplitude, in turn reduced by heating effects, when  $f$  exceeds a  
421 threshold fluence, thus stabilising the monoclinic metal, metastable at equilibrium.

422 In order to simulate the spatial dynamics of the laser-induced metalization, we start from the  
423 calculated shear strain map, reported in Fig. 8. As the pump excitation fluence rises, the concur-  
424 rent increase of  $\epsilon_{IMT}(f)$  leads to the possible nucleation of non-thermal metal regions with finite  
425 monoclinic shear strain, whenever the condition  $\epsilon_2(\mathbf{r}) \leq \epsilon_{IMT}(f)$  is met. In Fig. 10 we report  
426 the spatial configuration of such domains (purple areas), which are metallic and yet characterized  
427 by the same in-plane monoclinic nanotexture of the insulating phase (see Supplementary Mate-  
428 rial <sup>43</sup> for the parameters). We note that the non-thermal metal starts nucleating at the boundaries  
429 between different monoclinic twins, where, as previously discussed, the strain is constrained to  
430 smaller values than in the interior of each domain. As  $\epsilon_{IMT}(f)$  increases, the filling fraction of the  
431 non-thermal metal phase grows progressively up to the point of occupying the entire region.

432 **Time-resolved PEEM experiments** To demonstrate that such intriguing scenario indeed realises  
433 in photoexcited  $V_2O_3$ , we developed a novel time-resolved X-ray PEEM experiment (see Fig. 11)

434 with 30 nm and 80 ps spatial and temporal resolution (see Supplementary Material <sup>43</sup> for the ex-  
435 perimental details). With this imaging method we studied the temporal response of the monoclinic  
436 domains triggered by a properly synchronized pulsed laser excitation (1.5 eV photon energy;  $\sim 50$   
437 fs pulse duration) capable of impulsively changing the  $e_g^\pi$  and  $a_{1g}$  band population and possibly  
438 inducing the non-thermal metallic monoclinic state.

439 The time-resolved experiments were performed on a 50 nm  $V_2O_3$  crystalline film deposited  
440 by oxygen-assisted molecular beam epitaxy on a sapphire substrate, with  $c$ -axis perpendicular  
441 to the surface <sup>45</sup>. In order to characterize the IMT, we first measured the temperature-dependent  
442 optical properties at a selected probe photon energy (2.4 eV) during the heating and cooling cycles.  
443 The curve reported in Fig. 12a shows the typical hysteresis of the insulator to metal transition with  
444 mid-point at  $T_c \simeq 140$  K, slightly smaller than that observed in bulk crystals as a consequence  
445 of the film residual strain <sup>45</sup>. The reflectivity at 2.4 eV drops by 14% when the temperature is  
446 increased from 100 K (insulating phase) to 180 K (metallic phase), while the film resistivity drops  
447 by approximately 3 orders of magnitude (see Supplementary Figure S2 <sup>43</sup>). Figs. 12b and 12c  
448 show equilibrium XLD-PEEM images of the sample taken at  $T=100$  K and 180 K, respectively.  
449 As discussed at length in Sec. 2 the XLD-PEEM images clearly evidence in the low temperature  
450 monoclinic phase the formation of stripe-like domains corresponding to different monoclinic twins  
451 <sup>37</sup>. When the temperature is increased well above  $T_c$ , the monoclinic nanotexture is replaced by a  
452 homogeneous corundum phase with almost absent XLD contrast.

453 As extensively discussed in the literature<sup>20,21,27,28,37,68,69</sup>, the electronic IMT can be also

454 photo-induced by using ultrashort infrared pulses as the external control parameter. When the ex-  
455 citation is intense enough, the insulating phase collapses on a timescale of  $\sim 30\text{-}50$  ps transforming  
456 into a new phase with the same optical properties as the metallic one. We monitored such trans-  
457 formation in our sample by recording the relative reflectivity variation after 100 ps between the  
458 optical pump and probe, i.e. when the time-resolved signal already reached a plateau (see Figure  
459 S3). In Fig. 12d we show the relative reflectivity variation at 2.4 eV probe photon energy as a func-  
460 tion of the impinging pump fluence. Above  $\approx 8\text{mJ}/\text{cm}^2$ , the measured reflectivity drop perfectly  
461 matches the equilibrium reflectivity difference between the insulating and metallic phases, thus  
462 demonstrating that the whole of the pumped volume is turned into the electronic metallic phase.

463 In order to investigate the dynamics of the monoclinic domains during the photoinduced  
464 insulator-to-metal transition, we performed a XLD-PEEM experiment exploiting the inherent pulse  
465 structure of the synchrotron X-ray radiation and the synchronization with a femtosecond laser  
466 source, which allows turning the XLD-PEEM experiment into a time-resolved microscopy tool  
467 with 80 ps time-resolution (see Supplementary Material <sup>43</sup>). The experiment was carried out on the  
468 same sample, and in the same experimental conditions as the optical pump-probe results reported  
469 in Fig. 12d, in order to avoid possible artefacts related to different average heating in the two  
470 experiments <sup>30</sup>. The pump-probe spatial and temporal overlap was carefully checked by exploiting  
471 the non-linear photoemission from surface impurities, as explained in detail in the Supplementary  
472 Material <sup>43</sup> (see Sec. S1). Fig. 13a displays a typical image of the monoclinic domains 150 ps  
473 before and 30 ps after the excitation with laser pulses at  $22\pm 4$  mJ/cm<sup>2</sup> fluence. Although the  
474 excitation exceeds by far the threshold necessary to photoinduce the complete transformation into

475 the electronic metallic phase, our results show that, despite a moderate smearing of the contrast  
476 due to a small residual average heating, the monoclinic nanotexture is fully retained. These results  
477 demonstrate that, upon photoexcitation, the system undergoes an electronic transformation from  
478 the insulating to a metal-like state, while maintaining the in-plane shear strain of the monoclinic  
479 phase. In Fig. 13c we report the long-time dynamics of the contrast between neighbouring domains  
480 as a function of the time delay between the infrared pump and the X-ray probe. The photoinduced  
481 signal recovers within 3 ns, which corresponds to the cooling time of the sample<sup>9</sup>. No signature  
482 of long-time melting of the monoclinic nanotexture is observed.

483 A possible route to control the non-thermal metallic phase is given by interface strain engi-  
484 neering<sup>70</sup>, which allows to control the residual interface strain in the  $V_2O_3$  film. Quite naturally,  
485 the presence of residual tensile strain in the film may enhance  $\epsilon_{IMT}$  and favour the emergence of  
486 monoclinic metallic regions. In Fig. 14a we compare the fluence dependent filling fraction mea-  
487 sured on the  $V_2O_3$  film used for tr-PEEM measurements to that obtained on a similar  $V_2O_3$  film  
488 in which the residual strain is diminished by means of a  $Cr_2O_3$  buffer layer (see Section S2 of the  
489 Supplementary Material<sup>43</sup>)<sup>45</sup>. The fluence dependent data show a remarkably different metalliza-  
490 tion dynamics, compatible with a decrease of  $\epsilon_{IMT}$  in the film with the  $Cr_2O_3$  buffer layer. We  
491 underline that, in both cases, the morphology of monoclinic domains is very similar, as shown by  
492 PEEM images (see Fig. S4). The difference in the  $\epsilon_{IMT}$  values does not impact on the monoclinic  
493 nanotexture, which is governed by the functional (9), but rather controls the fragility toward the  
494 emergence of the photo-induced non-thermal metallic phase. In Fig. 14b we present more data  
495 points showing the correlation between residual tensile strain and the value of  $\epsilon_{IMT}$ .

## 496 **5 Conclusions**

497 In this work, we have developed a coarse-grained model, based on the minimization of a Landau-  
498 Ginzburg energy functional, to account for the space-dependent lattice and electronic dynamics  
499 across the insulator-to-metal transition in the archetypal Mott insulator  $V_2O_3$ . The spontaneous  
500 long-range nanotexture, originated by the minimization of the lattice energy, emerges as a key ele-  
501 ment to describe both the temperature-driven and the photoinduced transition. The reduced-strain  
502 regions at the domain boundaries and corners provide the necessary template for the nucleation of  
503 metallic domains. In out-of-equilibrium conditions, the domain boundaries stabilize and protect  
504 the photoinduced non-thermal monoclinic metallic state, which would be unstable at equilibrium  
505 an in homogeneous systems.

506 Although the reported theory and experiments refer to the Mott transition in  $V_2O_3$ , the  
507 present results unveil a profound and general link between the real-space topology, the transi-  
508 tion dynamics and the emergence of non-thermal electronic states in quantum materials. The  
509 combination of multiscale modeling and microscopy experiments with time-resolution offers new  
510 platforms to understand and control the transition dynamics of solids which exhibit spontaneous  
511 self-organization at the nanoscale. Indeed the complexity of space-dependent solid-solid phase  
512 transformations involving different degrees of freedom (electrons, lattice, spins, etc.) opens new  
513 exciting possibilities for achieving the full control of the transition and for synthesizing novel  
514 emerging metastable states that do not exist at equilibrium and in homogeneous phases. The com-  
515 bination of real-space morphology control via interface engineering, electric fields or pressure,

516 with the development of novel excitation schemes to coherently manipulate insulator to metal  
517 phase transitions <sup>71</sup> are expected to open new routes for achieving the full and reversible control of  
518 the electronic properties of correlated oxides.

519 From the theoretical side, our results call for the development of realistic models that capture  
520 the long-range dynamics and complexity of electronic transitions, which are usually tackled start-  
521 ing from a microscopic approach. Experimentally, the present results justify the ongoing efforts to  
522 develop novel table-top and large-scale facility time-resolved microscopy techniques to investigate  
523 the intertwining between non-thermal properties and real-space morphology in quantum corre-  
524 lated materials. Addressing the role of real space inhomogeneities and intrinsic strain nanotexture  
525 will be crucial to finally clarify the long-standing issue about the possibility of fully decoupling  
526 and control the electronic and structural phase transitions in vanadates <sup>3, 25, 26, 29, 30, 69, 72–74</sup> and other  
527 Mott materials.

## 528 **Acknowledgments**

529 C.G., A.R. and P.F. acknowledge financial support from MIUR through the PRIN 2015 (Prot.  
530 2015C5SEJJ001) and PRIN 2017 (Prot. 20172H2SC4\_005) programs. C.G. and G.F. acknowl-  
531 edge support from Università Cattolica del Sacro Cuore through D.1, D.2.2, and D.3.1 grants.  
532 We acknowledge Diamond Light Source for the provision of beamtime under proposals num-  
533 ber SI18897 and MM21700. JPL acknowledges financial supported by the KU Leuven Research  
534 Funds, Project No. KAC24/18/056, No. C14/17/080 and iBOF/21/084 as well as the Research

535 Funds of the INTERREG-E-TEST Project (EMR113) and INTERREG-VL-NL-ETPATHFINDER  
536 Project (0559). M.M. acknowledges support from "Severo Ochoa" Programme for Centres of Ex-  
537 cellence in R&D (MINCINN, Grant SEV-2016-0686). M.F. has received funding from the Euro-  
538 pean Research Council (ERC) under the European Union's Horizon 2020 research and innovation  
539 programme, Grant agreement No. 692670 "FIRSTORM".

- 540 1. Mott, N. F. The basis of the electron theory of metals, with special reference to the transition  
542 metals. *Proceedings of the Physical Society. Section A* **62**, 416 (1949). URL [http://stacks.iop.  
543 org/0370-1298/62/i=7/a=303](http://stacks.iop.org/0370-1298/62/i=7/a=303).
- 544 2. Fish, J., Wagner, G. J. & Keten, S. Mesoscopic and multiscale modelling in materials. *Nature*  
545 *Materials* **20**, 774–786 (2021).
- 546 3. McLeod, A. S. *et al.* Nanotextured phase coexistence in the correlated insulator  $V_2O_3$ . *Nature*  
547 *Physics* **13**, 80 (2016).
- 548 4. McLeod, A. S. *et al.* Nano-imaging of strain-tuned stripe textures in a Mott crystal. *npj*  
549 *Quantum Materials* **6**, 46 (2021).
- 550 5. Ronchi, A. *et al.* Ultrafast orbital manipulation and Mott physics in multi-band correlated  
551 materials. *Proc. SPIE* **17** (2018).
- 552 6. Stoliar, P. *et al.* Universal Electric-Field-Driven Resistive Transition in Narrow-Gap Mott  
553 Insulators. *Advanced Materials* **25**, 3222–3226 (2013).

- 554 7. Stoliar, P. *et al.* A Leaky-Integrate-and-Fire Neuron Analog Realized with a Mott Insulator.  
555 *Advanced Functional Materials* **27**, 1604740 (2017).
- 556 8. del Valle, J., Ramirez, J. G., Rozenberg, M. J. & Schuller, I. K. Challenges in materials and  
557 devices for resistive-switching-based neuromorphic computing. *Journal of Applied Physics*  
558 **124**, 211101 (2018).
- 559 9. Ronchi, A. *et al.* Light-Assisted Resistance Collapse in a  $V_2O_3$ -Based Mott-Insulator Device.  
560 *Phys. Rev. Applied* **15**, 044023 (2021).
- 561 10. Adda, C. *et al.* Mott insulators: A large class of materials for Leaky Integrate and Fire (LIF)  
562 artificial neuron. *Journal of Applied Physics* **124**, 152124 (2018).
- 563 11. Adda, C. *et al.* First demonstration of “Leaky Integrate and Fire” artificial neuron behavior on  
564  $(V_{0.95}Cr_{0.05})_2O_3$  thin film. *MRS Communications* **8**, 835–841 (2018).
- 565 12. Pérez-Toml’as, A. Functional Oxides for Photoneuromorphic Engineering: Toward a Solar  
566 Brain. *Advanced Materials Interfaces* **6**, 1900471 (2019).
- 567 13. Kim, H., Jo, Y., Kim, S., Kim, D. & Hur, J. 2g hts racetrack coil protection using smart  
568 switching feature of  $v_2o_3$ . *IEEE Transactions on Applied Superconductivity* **29**, 1–5 (2019).
- 569 14. Salev, P., del Valle, J., Kalcheim, Y. & Schuller, I. K. Giant nonvolatile resistive switching in  
570 a mott oxide and ferroelectric hybrid. *Proceedings of the National Academy of Sciences* **116**,  
571 8798–8802 (2019).

- 572 15. del Valle, J. *et al.* Subthreshold firing in mott nanodevices. *Nature* **569**, 388–392 (2019). URL  
573 <https://doi.org/10.1038/s41586-019-1159-6>.
- 574 16. Stoliar, P. *et al.* Universal Electric-Field-Driven Resistive Transition in Narrow-Gap Mott  
575 Insulators. *Advanced Materials* **25**, 3222–3226 (2013).
- 576 17. Rupp, J. A. J. *et al.* Different threshold and bipolar resistive switching mechanisms in re-  
577 actively sputtered amorphous undoped and Cr-doped vanadium oxide thin films. *Journal of*  
578 *Applied Physics* **123**, 044502 (2018).
- 579 18. Rúa, A. *et al.* Toward reproducible metal-insulator transition characteristics in V<sub>2</sub>O<sub>3</sub> thin films  
580 sputter-deposited on glass. *Journal of Applied Physics* **124**, 205301 (2018).
- 581 19. Wouters, D. J., Menzel, S., Rupp, J. A. J., Hennen, T. & Waser, R. On the universality of the  
582 i–v switching characteristics in non-volatile and volatile resistive switching oxides. *Faraday*  
583 *Discuss.* **213**, 183–196 (2019). URL <http://dx.doi.org/10.1039/C8FD00116B>.
- 584 20. Lantz, G. *et al.* Ultrafast evolution and transient phases of a prototype out-of-equilibrium  
585 Mott–Hubbard material. *Nature Communications* **8**, 13917 (2017). URL [https://doi.org/10.](https://doi.org/10.1038/ncomms13917)  
586 [1038/ncomms13917](https://doi.org/10.1038/ncomms13917).
- 587 21. Boschetto, D. *et al.* Reply to: Ultrafast evolution and transient phases of a prototype out-of-  
588 equilibrium Mott-Hubbard material. *Nature Communications* **10**, 4035 (2019). URL [https:](https://doi.org/10.1038/s41467-019-11744-2)  
589 [//doi.org/10.1038/s41467-019-11744-2](https://doi.org/10.1038/s41467-019-11744-2).

- 590 22. Giorgianni, F., Sakai, J. & Lupi, S. Overcoming the thermal regime for the electric-field  
591 driven Mott transition in vanadium sesquioxide. *Nature Communications* **10**, 1159 (2019).  
592 URL <https://doi.org/10.1038/s41467-019-09137-6>.
- 593 23. Kalcheim, Y. *et al.* Non-thermal resistive switching in Mott insulator nanowires. *Nature*  
594 *Communications* **11**, 2985 (2020).
- 595 24. Giorgianni, F., Sakai, J. & Lupi, S. Overcoming the thermal regime for the electric-field driven  
596 Mott transition in vanadium sesquioxide. *Nature Communications* **10**, 1159 (2019).
- 597 25. Morrison, V. R. *et al.* A photoinduced metal-like phase of monoclinic VO<sub>2</sub> revealed by ultra-  
598 fast electron diffraction. *Science* **346**, 445–448 (2014).
- 599 26. Otto, M. R. *et al.* How optical excitation controls the structure and properties of vanadium  
600 dioxide. *Proceedings of the National Academy of Sciences* **116**, 450–455 (2019).
- 601 27. Abreu, E. *et al.* Dynamic conductivity scaling in photoexcited V<sub>2</sub>O<sub>3</sub> thin films. *Phys. Rev. B*  
602 **92**, 085130 (2015).
- 603 28. Abreu, E. *et al.* Ultrafast electron-lattice coupling dynamics in VO<sub>2</sub> and V<sub>2</sub>O<sub>3</sub> thin films. *Phys.*  
604 *Rev. B* **96**, 094309 (2017).
- 605 29. Lantz, G. *et al.* Ultrafast evolution and transient phases of a prototype out-of-equilibrium  
606 Mott-Hubbard material. *Nature Communications* **8**, 13917 (2017).
- 607 30. Vidas, L. *et al.* Does VO<sub>2</sub> Host a Transient Monoclinic Metallic Phase? *Phys. Rev. X* **10**,  
608 031047 (2020).

- 609 31. McWhan, D. B., Rice, T. M. & Remeika, J. B. Mott transition in Cr-doped  $V_2O_3$ . *Phys. Rev.*  
610 *Lett.* **23**, 1384 (1969).
- 611 32. McWhan, D. B. & Remeika, J. P. Metal-insulator transition in  $(V_{1-x}Cr_x)_2O_3$ . *Phys. Rev. B* **2**,  
612 3734 (1970).
- 613 33. McWhan, D. B. *et al.* Electronic specific heat of metallic Ti-doped  $V_2O_3$ . *Phys. Rev. Lett.* **27**,  
614 941 (1971).
- 615 34. McWhan, D. B., Menth, A., Remeika, J. P., Rice, T. M. & Brinkman, W. F. Metal-insulator  
616 transitions in pure and doped  $V_2O_3$ . *Phys. Rev. B* **7**, 1920 (1973).
- 617 35. McLeod, A. S. *et al.* Nanotextured phase coexistence in the correlated insulator  $V_2O_3$ . *Nature*  
618 *Physics* **13**, 80–86 (2017). URL <https://doi.org/10.1038/nphys3882>.
- 619 36. Shao, Z. *Lattice Distortion of  $V_2O_3$  thin films during metal-to-insulator transition*. Master's  
620 thesis, Cornell University (2019). URL <https://hdl.handle.net/1813/67719>.
- 621 37. Ronchi, A. *et al.* Early-stage dynamics of metallic droplets embedded in the nanotextured  
622 Mott insulating phase of  $V_2O_3$ . *Phys. Rev. B* **100**, 075111 (2019). URL [https://link.aps.org/  
623 doi/10.1103/PhysRevB.100.075111](https://link.aps.org/doi/10.1103/PhysRevB.100.075111).
- 624 38. Ding, Y. *et al.* Novel High-Pressure Monoclinic Metallic Phase of  $V_2O_3$ . *Phys. Rev. Lett.* **112**,  
625 056401 (2014). URL <https://link.aps.org/doi/10.1103/PhysRevLett.112.056401>.
- 626 39. Bai, L. *et al.* Pressure-induced cation-cation bonding in  $V_2O_3$ . *Phys. Rev. B* **92**, 134106  
627 (2015). URL <https://link.aps.org/doi/10.1103/PhysRevB.92.134106>.

- 628 40. Chudnovskii, F. *et al.* Acoustic Emission during Metal-Insulator Phase Transition in  $V_2O_3$ .  
629 *Journal of Solid State Chemistry* **133**, 430 – 433 (1997). URL [http://www.sciencedirect.com/  
630 science/article/pii/S0022459697975034](http://www.sciencedirect.com/science/article/pii/S0022459697975034).
- 631 41. Dernier, P. D. & Marezio, M. Crystal structure of the low-temperature antiferromagnetic phase  
632 of  $V_2O_3$ . *Phys. Rev. B* **2**, 3771 (1970).
- 633 42. Fabrykiewicz, P., Przeniosło, R., Sosnowska, I. & Fauth, F. Positive and negative monoclinic  
634 deformation of corundum-type trigonal crystal structures of  $M_2O_3$  metal oxides. *Acta Crystal-*  
635 *lographica Section B* **74**, 660–672 (2018). URL <https://doi.org/10.1107/S2052520618014968>.
- 636 43. See the Supplementary Material at....
- 637 44. Poteryaev, A. I. *et al.* Enhanced crystal field splitting and orbital selective coherence by strong  
638 correlations in  $V_2O_3$ . *Phys. Rev. B* **76**, 085127 (2007).
- 639 45. Dillemans, L. *et al.* Evidence of the metal-insulator transition in ultrathin unstrained  $V_2O_3$   
640 thin films. *Applied Physics Letters* **104**, 071902 (2014).
- 641 46. Scholl, A. *et al.* Observation of Antiferromagnetic Domains in Epitaxial Thin Films. *Science*  
642 **287**, 1014–1016 (2000).
- 643 47. Tanaka, A. Electronic Structure and Phase Transition in  $V_2O_3$ : Importance of 3d Spin-Orbit  
644 Interaction and Lattice Distortion. *Journal of the Physical Society of Japan* **71**, 1091 (2002).

- 645 48. Grieger, D. & Fabrizio, M. Low-temperature magnetic ordering and structural distortions in  
646 vanadium sesquioxide  $V_2O_3$ . *Phys. Rev. B* **92**, 075121 (2015). URL [https://link.aps.org/doi/](https://link.aps.org/doi/10.1103/PhysRevB.92.075121)  
647 [10.1103/PhysRevB.92.075121](https://link.aps.org/doi/10.1103/PhysRevB.92.075121).
- 648 49. Fouet, J., Sindzingre, P. & Lhuillier, C. An investigation of the quantum  $J_1$ - $J_2$ - $J_3$  model on  
649 the honeycomb lattice. *The European Physical Journal B - Condensed Matter and Complex*  
650 *Systems* **20**, 241 (2001).
- 651 50. Albuquerque, A. *et al.* Phase diagram of a frustrated quantum antiferromagnet on the honey-  
652 comb lattice: Magnetic order versus valence-bond crystal formation. *Phys. Rev. B* **84**, 024406  
653 (2011).
- 654 51. Mezzacapo, F. & Boninsegni, M. Ground-state phase diagram of the quantum  $J_1$ - $J_2$  model on  
655 the honeycomb lattice. *Phys. Rev. B* **85**, 060402 (2012).
- 656 52. Leiner, J. C. *et al.* Frustrated Magnetism in Mott Insulating  $(V_{1-x}Cr_x)_2O_3$ . *Phys. Rev. X* **9**,  
657 011035 (2019). URL <https://link.aps.org/doi/10.1103/PhysRevX.9.011035>.
- 658 53. Pfalzer, P., Obermeier, G., Klemm, M., Horn, S. & denBoer, M. L. Structural precursor to the  
659 metal-insulator transition in  $V_2O_3$ . *Phys. Rev. B* **73**, 144106 (2006). URL [https://link.aps.org/](https://link.aps.org/doi/10.1103/PhysRevB.73.144106)  
660 [doi/10.1103/PhysRevB.73.144106](https://link.aps.org/doi/10.1103/PhysRevB.73.144106).
- 661 54. Kündel, J. *et al.* Direct observation of the lattice precursor of the metal-to-insulator transition  
662 in  $V_2O_3$  thin films by surface acoustic waves. *Applied Physics Letters* **102**, 101904 (2013).
- 663 55. Majid, S. S. *et al.* Stabilization of metallic phase in  $V_2O_3$  thin film. *Applied Physics Letters*  
664 **110**, 173101 (2017).

- 665 56. Singer, A. *et al.* Nonequilibrium Phase Precursors during a Photoexcited Insulator-to-Metal  
666 Transition in  $V_2O_3$ . *Phys. Rev. Lett.* **120**, 207601 (2018). URL [https://link.aps.org/doi/10.](https://link.aps.org/doi/10.1103/PhysRevLett.120.207601)  
667 [1103/PhysRevLett.120.207601](https://link.aps.org/doi/10.1103/PhysRevLett.120.207601).
- 668 57. Frandsen, B. A. *et al.* Intertwined magnetic, structural, and electronic transitions in  $V_2O_3$ .  
669 *Phys. Rev. B* **100**, 235136 (2019). URL [https://link.aps.org/doi/10.1103/PhysRevB.100.](https://link.aps.org/doi/10.1103/PhysRevB.100.235136)  
670 [235136](https://link.aps.org/doi/10.1103/PhysRevB.100.235136).
- 671 58. Kalcheim, Y. *et al.* Robust Coupling between Structural and Electronic Transitions in a Mott  
672 Material. *Phys. Rev. Lett.* **122**, 057601 (2019).
- 673 59. Rasmussen, K. O. *et al.* Three-Dimensional Elastic Compatibility and Varieties of Twins  
674 in Martensites. *Phys. Rev. Lett.* **87**, 055704 (2001). URL [https://link.aps.org/doi/10.1103/](https://link.aps.org/doi/10.1103/PhysRevLett.87.055704)  
675 [PhysRevLett.87.055704](https://link.aps.org/doi/10.1103/PhysRevLett.87.055704).
- 676 60. Shenoy, S. R., Lookman, T., Saxena, A. & Bishop, A. R. Martensitic textures: Multiscale  
677 consequences of elastic compatibility. *Phys. Rev. B* **60**, R12537–R12541 (1999). URL [https://](https://link.aps.org/doi/10.1103/PhysRevB.60.R12537)  
678 [link.aps.org/doi/10.1103/PhysRevB.60.R12537](https://link.aps.org/doi/10.1103/PhysRevB.60.R12537).
- 679 61. Vasseur, R., Lookman, T. & Shenoy, S. R. Microstructure from ferroelastic transitions using  
680 strain pseudospin clock models in two and three dimensions: A local mean-field analysis.  
681 *Phys. Rev. B* **82**, 094118 (2010). URL <https://link.aps.org/doi/10.1103/PhysRevB.82.094118>.
- 682 62. Nichols, D. N., Sladek, R. J. & Harrison, H. R. Elastic constants of  $V_2O_3$  between 300 and  
683 640 K: Anomalies near the high-temperature electrical transition. *Phys. Rev. B* **24**, 3025–3030  
684 (1981). URL <https://link.aps.org/doi/10.1103/PhysRevB.24.3025>.

- 685 63. Yang, H., Sladek, R. & Harrison, H. Shear elastic constant softening in  $V_{1-x}Cr_x)_2O_3$ : Second-  
686 order nature of the low temperature phase transition. *Solid State Communications* **47**, 955 –  
687 957 (1983). URL <http://www.sciencedirect.com/science/article/pii/0038109883909778>.
- 688 64. Yang, H. & Sladek, R. J. Elastic anomalies in  $(V_{1-x}Cr_x)_2O_3$ : Electron-transfer effects. *Phys.*  
689 *Rev. B* **34**, 2627–2631 (1986). URL <https://link.aps.org/doi/10.1103/PhysRevB.34.2627>.
- 690 65. Boccara, N. Second-order phase transitions characterized by a deformation of the unit cell.  
691 *Annals of Physics* **47**, 40 – 64 (1968). URL [http://www.sciencedirect.com/science/article/pii/](http://www.sciencedirect.com/science/article/pii/000349166890225X)  
692 000349166890225X.
- 693 66. Yethiraj, M., Werner, S. A., Yelon, W. B. & Honig, J. M. Phonon anomalies and the magnetic  
694 transition in pure and Cr-doped  $V_2O_3$ . *Phys. Rev. B* **36**, 8675–8686 (1987). URL [https://](https://link.aps.org/doi/10.1103/PhysRevB.36.8675)  
695 [link.aps.org/doi/10.1103/PhysRevB.36.8675](https://link.aps.org/doi/10.1103/PhysRevB.36.8675).
- 696 67. Shenoy, S. R. & Lookman, T. Strain pseudospins with power-law interactions: Glassy textures  
697 of a cooled coupled-map lattice. *Phys. Rev. B* **78**, 144103 (2008). URL [https://link.aps.org/](https://link.aps.org/doi/10.1103/PhysRevB.78.144103)  
698 [doi/10.1103/PhysRevB.78.144103](https://link.aps.org/doi/10.1103/PhysRevB.78.144103).
- 699 68. Liu, M. K. *et al.* Photoinduced Phase Transitions by Time-Resolved Far-Infrared Spectroscopy  
700 in  $V_2O_3$ . *Phys. Rev. Lett.* **107**, 066403 (2011).
- 701 69. Singer, A. *et al.* Nonequilibrium Phase Precursors during a Photoexcited Insulator-to-Metal  
702 Transition in  $V_2O_3$ . *Phys. Rev. Lett.* **120**, 207601 (2018).

- 703 70. Homm, P., Menghini, M., Seo, J. W., Peters, S. & Locquet, J. P. Room temperature Mott  
704 metal-insulator transition in  $V_2O_3$  compounds induced via strain-engineering. *APL Materials*  
705 **9**, 021116 (2021).
- 706 71. Horstmann, J. G. *et al.* Coherent control of a surface structural phase transition. *Nature* **583**,  
707 232–236 (2020).
- 708 72. Nájera, O., Civelli, M., Dobrosavljević, V. & Rozenberg, M. J. Resolving the  $VO_2$  contro-  
709 versy: Mott mechanism dominates the insulator-to-metal transition. *Phys. Rev. B* **95**, 035113  
710 (2017).
- 711 73. Kalcheim, Y. *et al.* Robust Coupling between Structural and Electronic Transitions in a Mott  
712 Material. *Phys. Rev. Lett.* **122**, 057601 (2019).
- 713 74. Frandsen, B. A. *et al.* Intertwined magnetic, structural, and electronic transitions in  $V_2O_3$ .  
714 *Phys. Rev. B* **100**, 235136 (2019).
- 715 75. McWhan, D. B. *et al.* Electronic specific heat of metallic ti-doped  $v_2O_3$ . *Phys. Rev. Lett.* **27**,  
716 941–943 (1971). URL <https://link.aps.org/doi/10.1103/PhysRevLett.27.941>.
- 717 76. Park, J.-H. *et al.* Spin and orbital occupation and phase transitions in  $V_2O_3$ . *Phys. Rev. B* **61**,  
718 11506–11509 (2000).

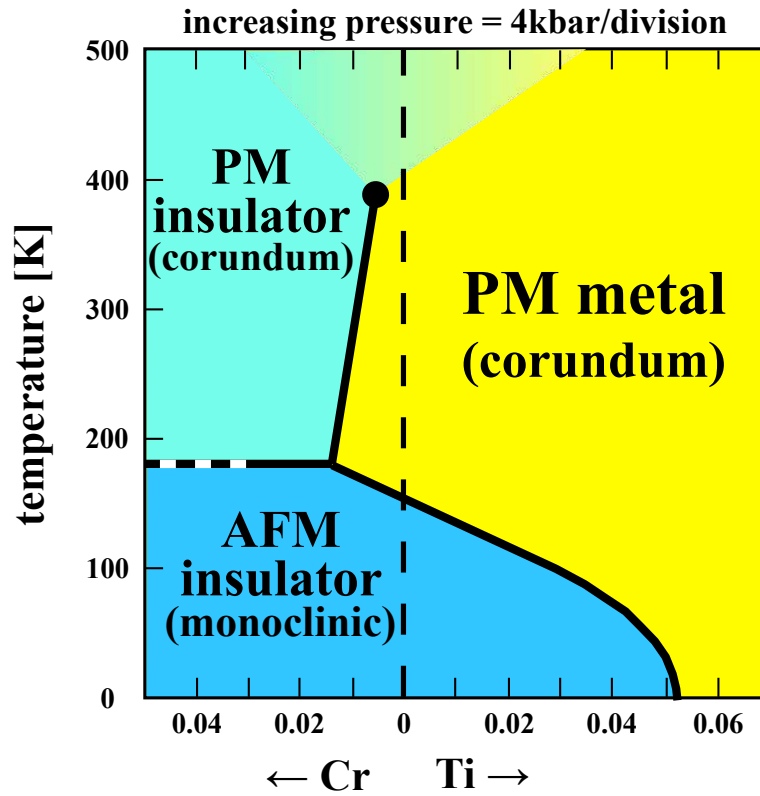


Figure 1: Phase diagram of  $(V_{1-x}M_x)_2O_3$ , with  $M=Cr, Ti$ , as function of the doping concentration  $x$  and pressure, from Ref. <sup>75</sup>. AFM and PM stand for antiferromagnetic and paramagnetic, respectively. All transition lines (solid black lines) are first order, with the one separating PM metal from PM insulator that terminates into a second order critical point (black dot). For Cr doping  $x \gtrsim 0.03$  there are evidences <sup>66</sup> that the transition becomes continuous, or very weakly first order, thus the dashed line.

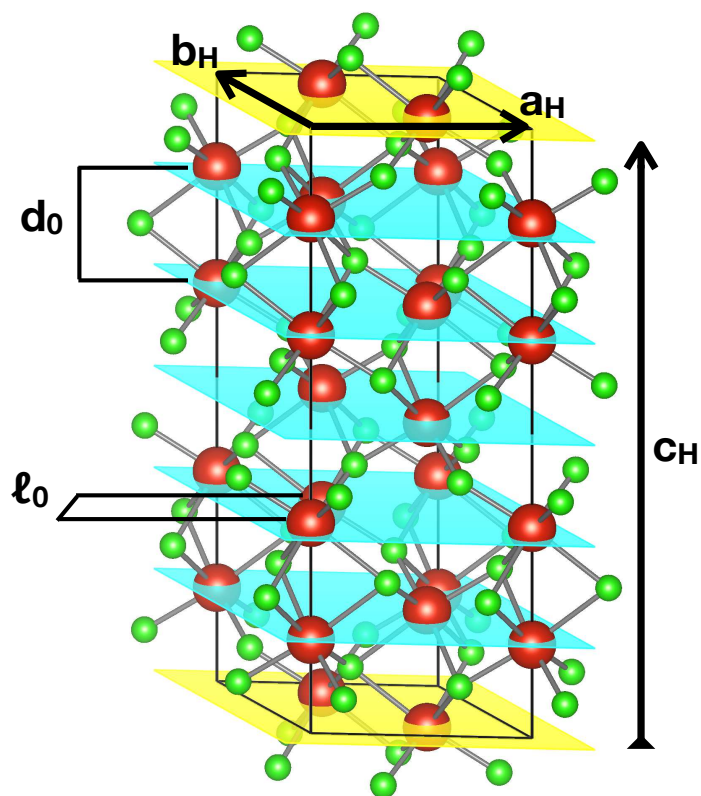


Figure 2: Non-primitive hexagonal unit cell of the high temperature corundum phase. Vanadium is shown in red, while oxygen in green. Note the alternating displacement of the V atoms off the honeycomb planes. The V-V nearest neighbour distance within the  $a_H - b_H$  plane,  $l_0$ , and along  $c_H$ ,  $d_0$ , are also shown.

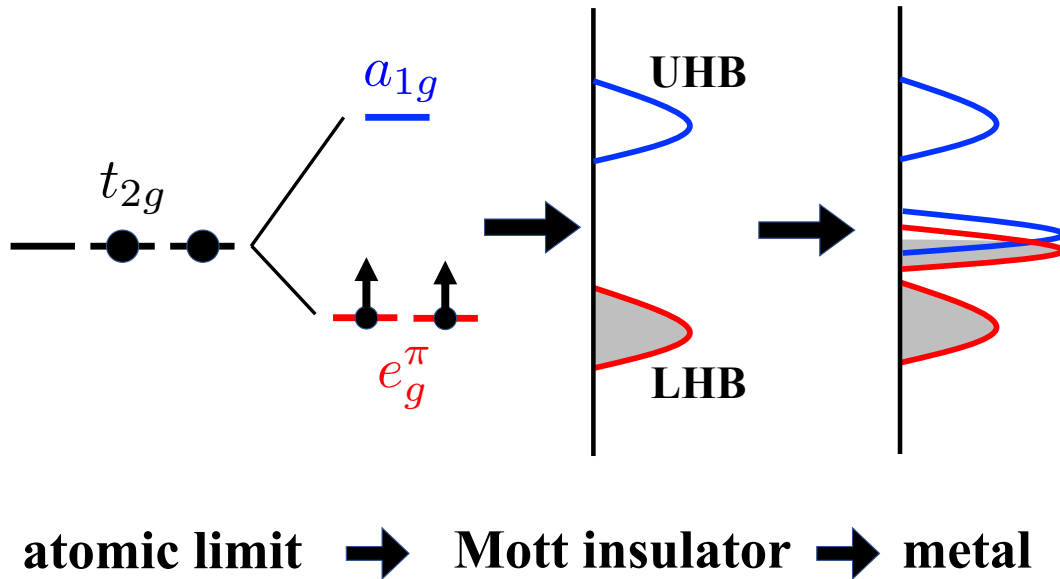


Figure 3: Sketch of the electronic Mott transition in  $V_2O_3$ . In the atomic limit, the two conduction electrons of  $V^{3+}$  occupy the  $t_{2g}$  orbital of the cubic-field split  $3d$ -shell. Because of the additional trigonal field, the  $t_{2g}$  triplet is further split into a lower  $e_g^\pi$  doublet and higher  $a_{1g}$  singlet. The two electrons thus sit into the  $e_g^\pi$  orbital, in a spin triplet configuration because of Hund's rules. In the solid state, this picture remains to a great extent unaltered inside the antiferromagnetic Mott insulator: the atomic levels broaden into lower and upper Hubbard bands, LHB and UHB, respectively. The spin-polarised LHB has prevailing  $e_g^\pi$  character (actually, the  $e_g^\pi:a_{1g}$  population ratio is 2:1<sup>76</sup>), while the empty UHB has dominant  $a_{1g}$  character. In the metal phase, quasiparticle bands appear at the Fermi level. Since the trigonal field weakens<sup>44</sup>, these bands overlap, thus a metallic behaviour with the simultaneous disappearance of magnetism.

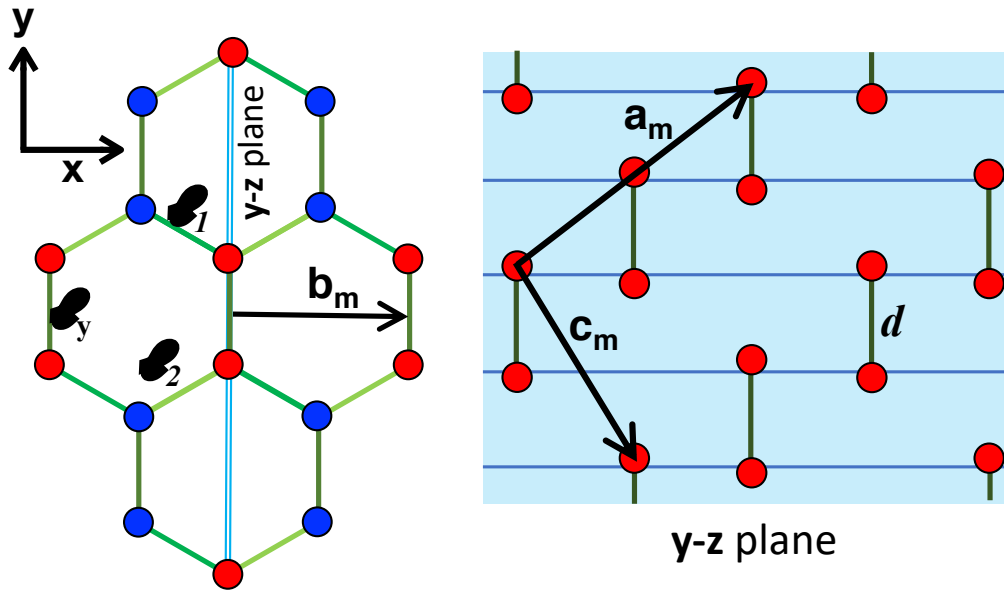


Figure 4: Magnetic order in the hexagonal plane, left panel, and in the  $y - z$  plane, equivalent to the  $a_m - c_m$  one, right panel. Red and blue circles correspond to V atoms with opposite spin. In the hexagonal plane we also draw the nearest neighbour bond lengths:  $l_y$ , which is ferromagnetic, and  $l_1$  and  $l_2$ , both antiferromagnetic. The dimers, with bond length  $d$ , lie in the  $y - z$  plane and are ferromagnetic, see left panel, where we also show the monoclinic lattice vectors  $a_m$  and  $c_m$ .

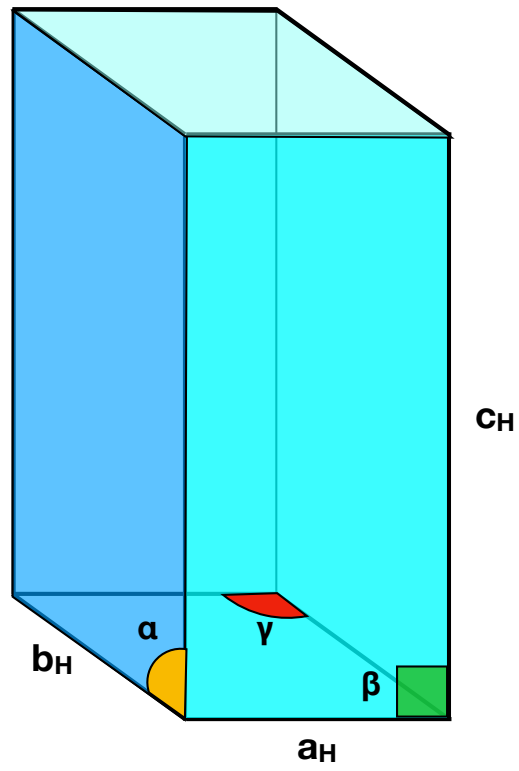


Figure 5: Pseudo-hexagonal unit cell that we use throughout this work.

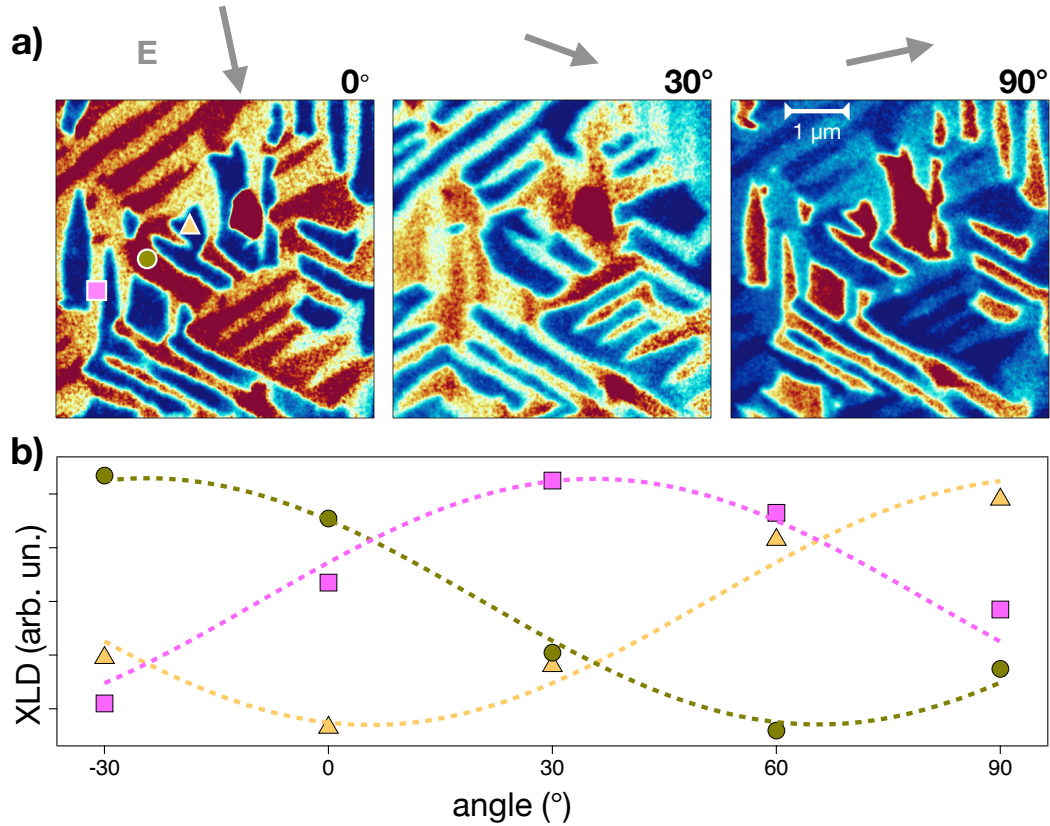


Figure 6: a) XLD-PEEM images taken at 100 K evidencing striped monoclinic domains characterized by different XLD intensity. The three distinct domains (red, blue, yellow), reflect the three possible monoclinic distortions along the equivalent edges of the vanadium hexagons within the honeycomb planes. The XLD signal, as demonstrated in the Supplementary Section S5<sup>43</sup>, crucially depends on the orientation between the electromagnetic polarization (grey arrows on top of the images) and the direction of the monoclinic distortion. The three panels show images taken for different polarization angles of the impinging X-ray pulses. The angle indicated refers to the initial (left panel) polarization, which is taken as reference. Note that in the left panel a small angle between the polarization direction and the  $y$ -axis, as defined in Fig. 4, is present in order to better highlight the three distinct domains. b) XLD signal as a function of the angle between the X-ray polarization and the sample axis. The pink square, green circle and yellow triangle refer to the positions indicated in panel a). Within each domain, the XLD signal displays the expected 180° periodicity. When comparing the three distinct domains, the XLD signal shows a 60° phase shift.

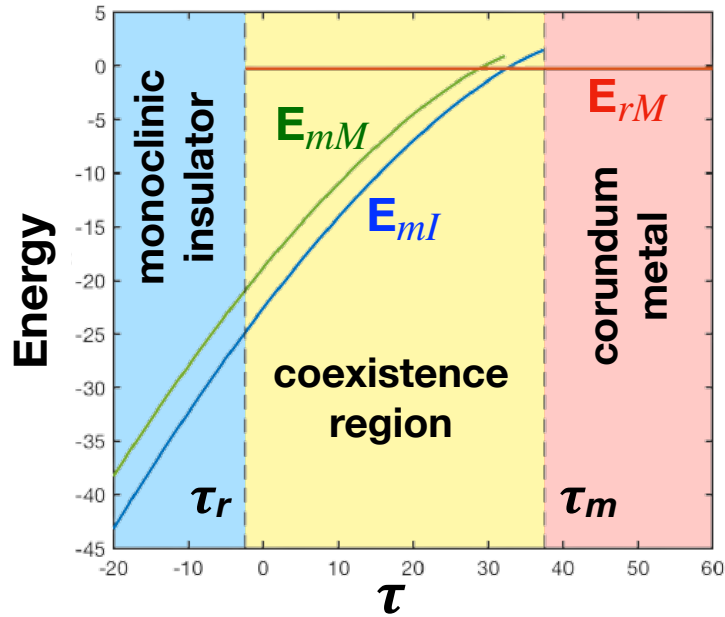


Figure 7: Phase diagram of the energy functional (14) as function of  $\tau$  assuming homogeneous phases.  $E_{rM}$ ,  $E_{mM}$  and  $E_{mI}$  are, respectively, the energies of the rhombohedral metal, red line, monoclinic metal, green line, and monoclinic insulator, blue line. The energy crossing between  $E_{rM}$  and  $E_{mI}$  signals the actual first order transition. The vertical dashed lines at  $\tau = \tau_m$  and  $\tau = \tau_r$  are, respectively, the monoclinic and rhombohedral spinodal points. For  $\tau \in [\tau_r, \tau_m]$  there is phase coexistence. We note the existence of a metastable monoclinic metal, with energy  $E_{mM}$ .

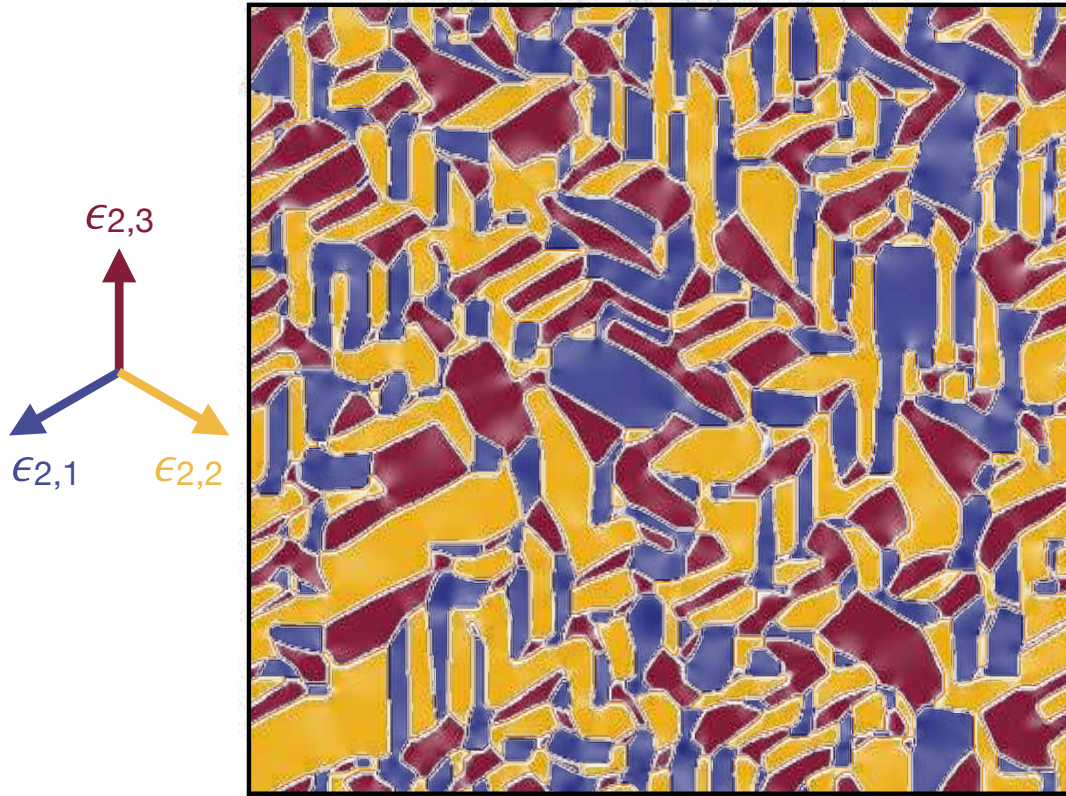


Figure 8: Calculated real space distribution of the shear strain  $\epsilon_2(\mathbf{r})$  deep inside the monoclinic insulating phase. The colours correspond to the three equivalent shear strain vectors  $\epsilon_{2,i}$ ,  $i = 1, 2, 3$ , shown on the left, which characterise the three equivalent monoclinic twins, see Eq. (7). For each domain, the intensity of the color is proportional to the strain amplitude. Lighter regions indicate a reduced strain amplitude. The interfaces between different domains evidently satisfy the curl-free condition (12).

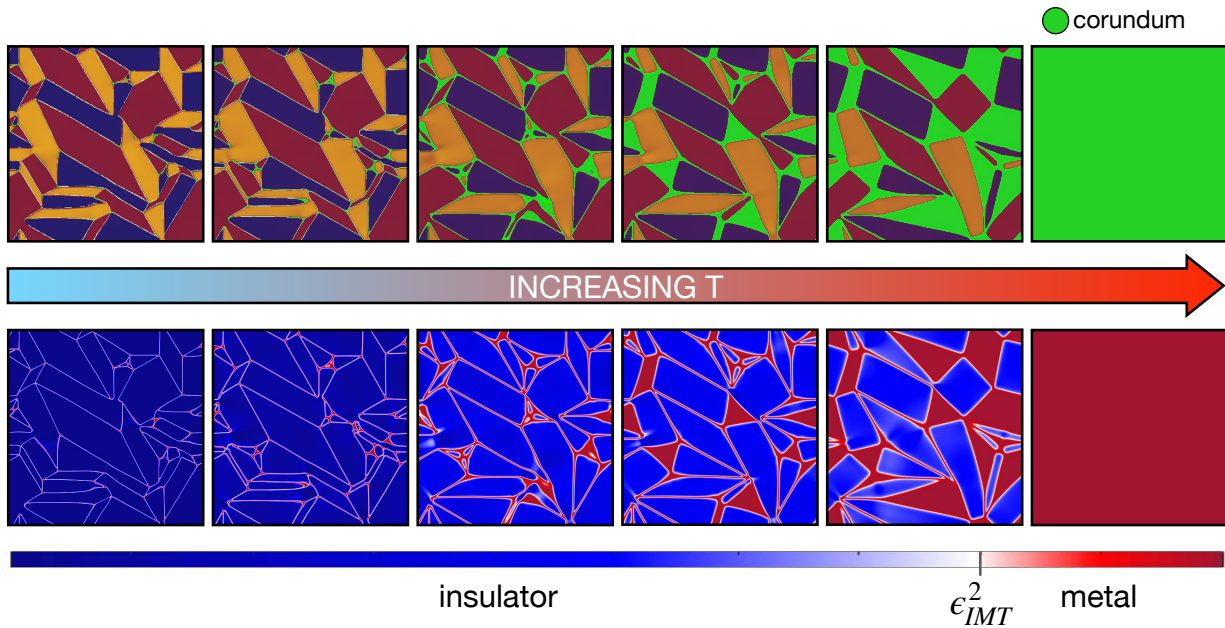


Figure 9: Calculated domain pattern across the first order transition upon rising temperature. Top panel: colour map of the shear strain  $\epsilon_2(\mathbf{r})$ , specifically, the monoclinic domains are indicated by the same colorscale (red, blue, yellow) as that used in Fig. 8. The rhombohedral domains are indicated in green. Bottom panel: colour map of the square modulus of the shear strain  $\epsilon_2(\mathbf{r})^2$ . Blue keys indicate the monoclinic insulating domains,  $\epsilon_2(\mathbf{r})^2 > \epsilon_{IMT}^2$ , while red keys the metallic ones,  $\epsilon_2(\mathbf{r})^2 < \epsilon_{IMT}^2$ .

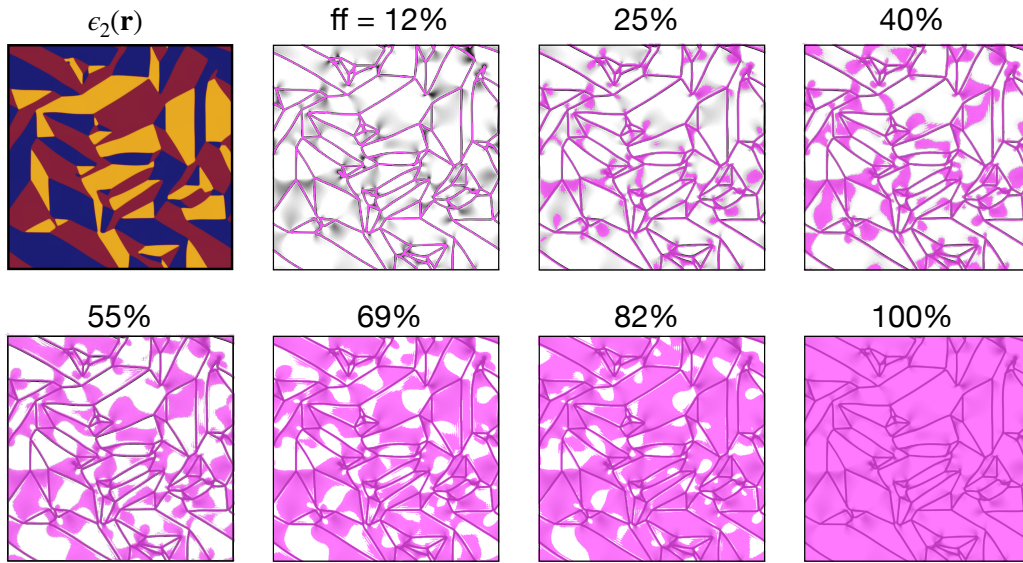


Figure 10: Map of the space-dependent calculated shear strain amplitude (grey color-scale) and metastable monoclinic metallic regions (purple). Darker grey indicates smaller strain amplitude. The purple areas highlight the spatial regions in which the electronic metallic solution with monoclinic strain is the stable one (absolute minimum in the free-energy), i.e. when the condition  $\epsilon_2(\mathbf{r}) \leq \epsilon_{IMT}(f)$  is fulfilled. We stress that in all panels the same monoclinic shear strain,  $\epsilon_2(\mathbf{r})$ , as that shown in top-left panel (same color scale as Fig. 8) is retained, although not shown for clarity. The filling fraction of the photo-induced non-thermal metallic phase is indicated for each panel.

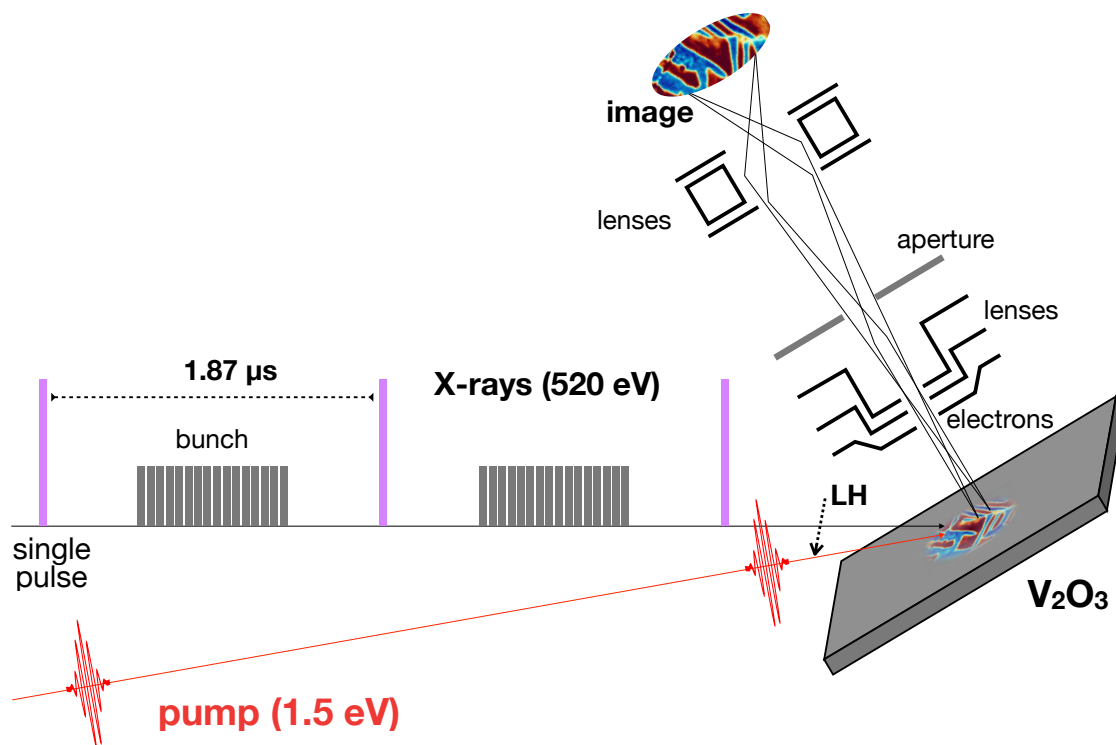


Figure 11: Cartoon of the time-resolved PEEM experiment. The signal originated by isolated X-rays pulses with linear horizontal (LH) polarization is collected by suitable synchronized gating of the X-ray detector. In order to optimize the signal and remove possible artifacts, each reported image is the difference between images taken with X-ray pulses at 520 eV, for which the contrast between signals from different monoclinic distortions is maximum, and 518 eV, for which the contrast is minimum<sup>37,76</sup>. The pump infrared laser is synchronized to the synchrotron pulses. The electrostatic lenses image the electrons photoemitted from the sample onto the detector.

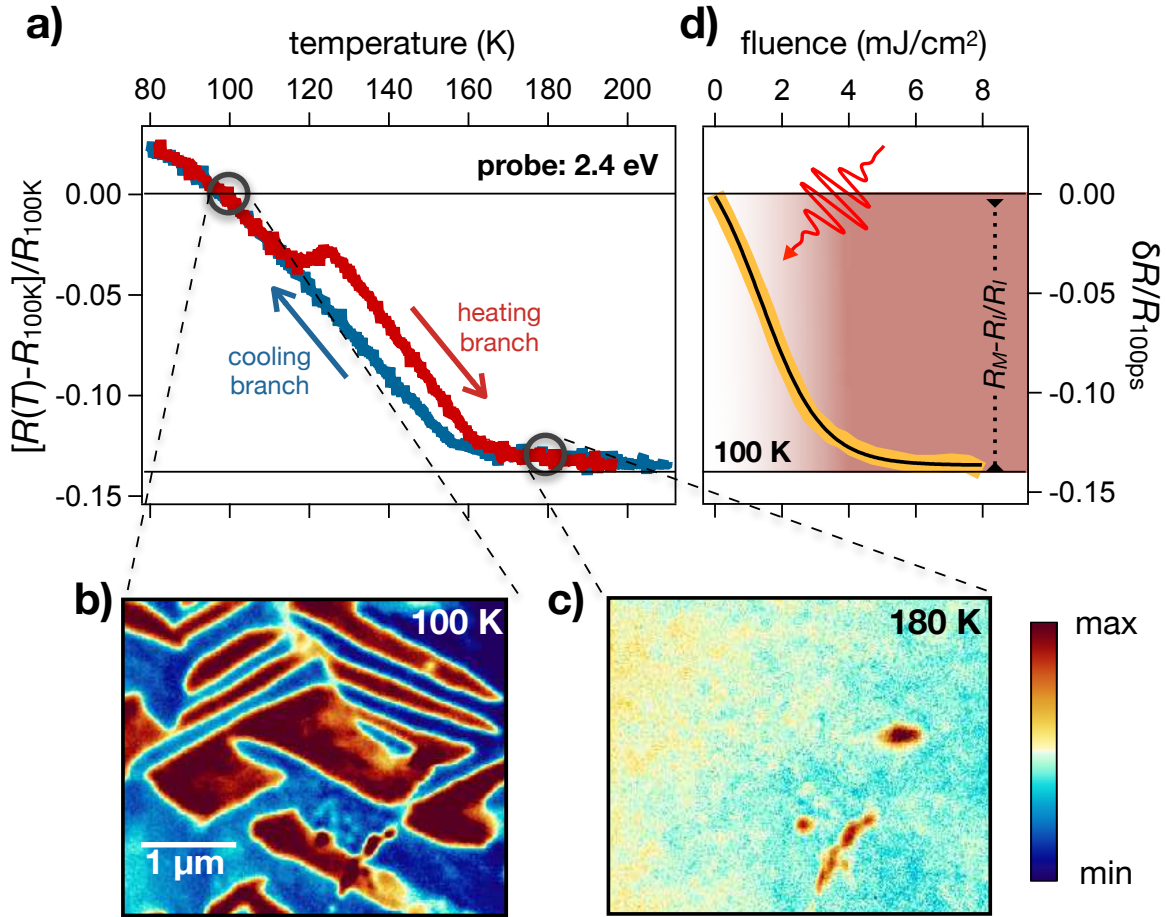


Figure 12: **a)** Reflectivity change of the  $V_2O_3$  crystal across the temperature-driven insulator-to-metal phase transition. The sample reflectivity is measured at 2.4 eV photon energy as a function of the sample temperature during the heating (red curve) and cooling (blue curve) processes. The graph displays the relative reflectivity variation with respect to the reflectivity measured at  $T=100$  K. **b)** PEEM image taken at 100 K evidencing stripe-like domains corresponding to the different monoclinic distortions. Note that the experimental configuration of the image shown (polarization parallel to one of the hexagon edges) is such that only two domains are visible. **c)** PEEM image taken at 180 K evidencing a homogeneous background, typical of the metallic corundum phase. The color scale indicates the amplitude of the PEEM signal. **d)** The asymptotic value of the relative reflectivity variation (yellow trace), i.e.  $\delta R/R(100\text{ ps})=[R(\Delta t=100\text{ ps})-R(\Delta t=0\text{ ps})]/R(\Delta t=0\text{ ps})$  where  $\Delta t$  is the pump-probe delay, is measured at 2.4 eV probe photon energy and  $T=100$  K as a function of the incident pump fluence. The black solid line is a guide to the eye.

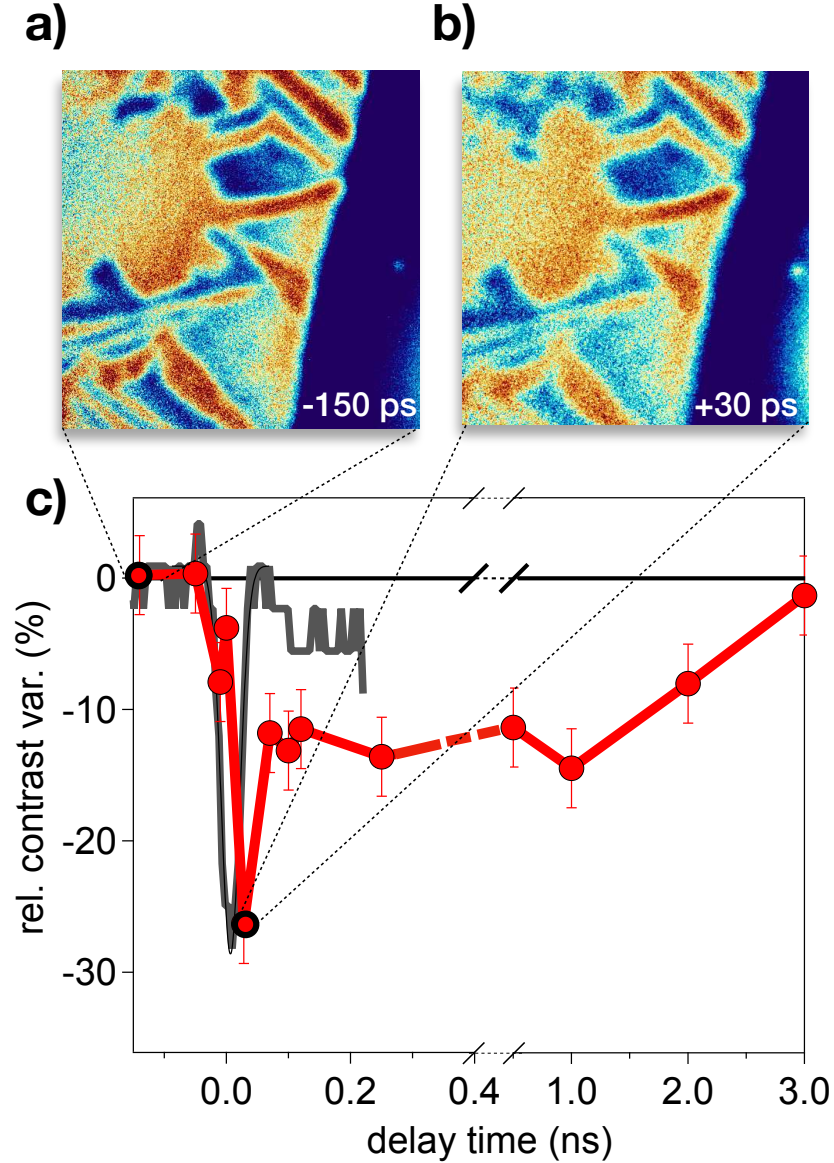


Figure 13: **a)** Time-resolved PEEM image taken at  $T=100$  K and at negative delay (-150 ps) between the infrared pump and the X-ray probe pulses. **b)** Time-resolved PEEM image taken at  $T=100$  K and at positive delay (+30 ps) between the infrared pump and the X-ray probe pulses. The color scale for both panels a) and b) is the same than that used in Fig. 12. **c)** Relative contrast (see the Supplemental Material <sup>43</sup>) between different domains as a function of the delay between the infrared pump and the X-ray probe pulses. The error bar accounts for the average fluctuation of the signal within the domains considered for the calculation of the relative contrast. The grey solid line is the cross correlation between the infrared pump and the X-ray probe pulses measured by exploiting the non-linear photoemission from surface impurities on the sample (see the Supplementary Material <sup>43</sup>).

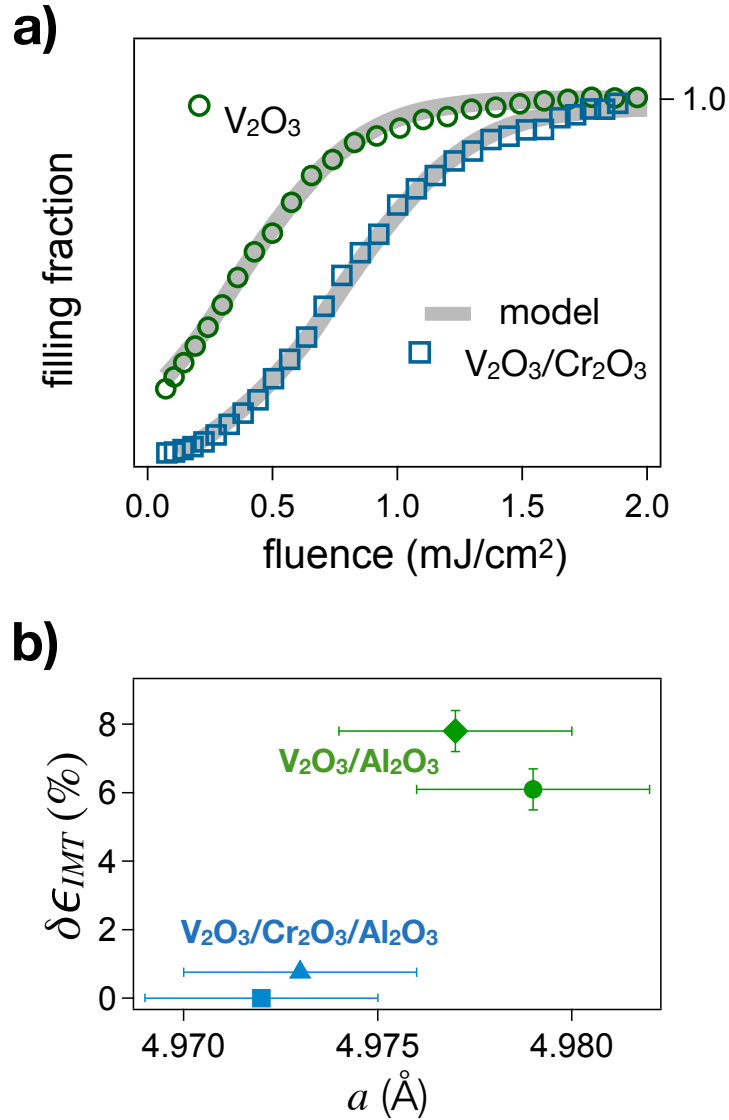


Figure 14: **a)** Metallic filling fraction, retrieved from the asymptotic value of the relative reflectivity variation, i.e.  $\delta R/R(100 \text{ ps})$ , as a function of the pump incident fluence for a 50 nm V<sub>2</sub>O<sub>3</sub> film directly grown on the sapphire substrate (green circles) and for a 55 nm V<sub>2</sub>O<sub>3</sub> film grown on a 60 nm Cr<sub>2</sub>O<sub>3</sub> buffer layer (blue squares). The grey solid lines represent the numerical filling fractions, calculated as the ratio between non-thermal metallic areas (purple areas in Fig. 10)) and the total area. **b)** Values of the estimated critical strain variation  $\delta\epsilon_{IMT}$ , calculated with respect to the reference sample V<sub>2</sub>O<sub>3</sub>/Cr<sub>2</sub>O<sub>3</sub>/Al<sub>2</sub>O<sub>3</sub> (55 nm/60 nm/substrate).  $\delta\epsilon_{IMT}$  is plotted as a function of the room temperature  $a$ -axis lattice parameter, as measured by X-ray diffraction, for samples with (blue points) and without (green points) the Cr<sub>2</sub>O<sub>3</sub> buffer layer. The symbols refer to the following samples: blue square V<sub>2</sub>O<sub>3</sub>/Cr<sub>2</sub>O<sub>3</sub>/Al<sub>2</sub>O<sub>3</sub> (55 nm/60 nm/substrate); blue triangle V<sub>2</sub>O<sub>3</sub>/Cr<sub>2</sub>O<sub>3</sub>/Al<sub>2</sub>O<sub>3</sub> (67 nm/40 nm/substrate); green diamond V<sub>2</sub>O<sub>3</sub>/Al<sub>2</sub>O<sub>3</sub> (40 nm/substrate); green circle V<sub>2</sub>O<sub>3</sub>/Al<sub>2</sub>O<sub>3</sub> (50 nm/substrate).

## Supplementary Files

This is a list of supplementary files associated with this preprint. Click to download.

- [supplementary.pdf](#)